Gain Dynamics of the N_2^+ Air Laser

Patrick Laferri$\grave{e}$re

A thesis submitted in partial fulfillment of the
requirements for the degree of

Master of Science

Department of Physics
University of Ottawa

Abstract

Lasing from femtosecond laser filaments is a relatively new field of study that has been studied since its first observation in 2003. Such lasing effect is of interest to the scientific community due to its possible application in remote sensing. This thesis studies the lasing dynamics of the excited molecular nitrogen ion N_2^+ which emits primarily at 391 nm and 428 nm wavelengths. We start by studying the ellipticity dependence of the gain from filaments in ambient air. We then study the ellipticity dependence in a vacuum in a supersonic gas jet to remove the complexity of filamentation. We show that recollision doesn't play a significant role in creating a population inversion by comparing the ellipticity dependence of the gain and high harmonic generation. The rest of this thesis is devoted to shining some light on another possible mechanism. We characterize the gain by its temporal profile, jet position dependence, and density dependence.

Acknowledgements

I would like to start by thanking my supervisor Dr. Paul Corkum who welcomed me in his group during the summer of 2015. I was given the opportunity to help move a home built chirped pulse amplification system from the National Reseach Council to the new Extreme Photonics Laboratory at the university. He then assigned me to work on the air lasing project with Mathiew Britton. Meetings with Paul are always very informative, and his ideas and suggestions are always helpful.

A huge thanks to Mathiew who tolerated me for over nine beam times of nearly three weeks each. We worked side by side in the lab since the start. Mathiew thought me almost everything I know about working in a laser lab. Whether it's during regular work hours or late at night, he is always ready to help. I cannot thank him enough for his contribution to my development as an experimentalist.

I would also like to thank Dr. Ladan Arissian who brought a lot of enthusiasm to our team. Ladan always brings fruitful discussions during meetings and makes time out of her busy schedule to come to the lab. I can't forget the contribution of our lab engineer Tyler Clancy who was always ready to help us along the way. He created the LabVIEW programs that we use to collect data. Although more complicated than needed, and nearly impossible to make changes to it, we do appreciate it. Tyler, unfortunately, left the group about a year ago. He has then been replaced by Vicky Wang, who has been amazing as well.

Discloser

I am not the sole contributor of the analyzed data in my thesis. Mathiew Britton, a PhD student, analyzed all the data in Section 4 (N_2^+ lasing in filaments). I did not reproduce them; I only manipulated the .fig files to present them here for completion. Mathiew also created the MATLAB analysis programs that we use on a daily basis. Most of the results presented in my thesis uses his code with small modifications. I was, however, involved in taking all the data presented in my thesis as well as setting up, aligning, and optimizing.

Publication related to the thesis

Mathew Britton, **Patrick Laferriere**, Dong Hyuk Ko, Zhengyan Li, Fanqi Kong, Graham Brown, Andrei Naumov, Chunmei Zhang, Ladan Arissian, and P. B. Corkum. Testing the role of recollision in N_2^+ air lasing. Physical Review Letters, 120(133208), 2018.

Section four (N_2^+ lasing in filaments) is covered in this publication as well as the majority of section five (The role of recollision in N_2^+ air lasing} presented in this thesis. Section 6 (N_2^+ lasing in a thin gas jet) covers material that is subject to future publications.

List of Figures

Contents

1 Introduction

1.1 Introduction to air lasing

The invention of the laser in 1960[14] led to the development of a variety of laser-spectroscopic techniques for diagnostic purposes. These methods are extremely valuable for probing harsh environments such as combustion processes, where the high spatial and temporal resolution provided by optical techniques are particularly useful. Usually, when we talk about lasers, it is referred to as an instrument made of various optical elements which include a gain medium, a pump source, and an optical resonator. Placing lasers at the required location can be problematic. For example, to improve techniques in remote sensing such as Light Detection and Ranging (LIDAR), a laser would have to be placed behind the region of interest so that we may analyze the forward propagating lasing emission from a ground base station.

In 2003, Q. Luo et *al.* studied the backscattered fluorescence of molecular nitrogen from filaments in air generated from ultrafast Ti:sapphire femtosecond laser pulses and found that lasing from nitrogen in air is possible in the forward and backward direction[15]. The conclusion about this lasing effect was drawn from the exponential growth of the fluorescence yield around 357 nm wavelength (corresponding to the $C^3\Pi_u(\nu = 0)$ to $B^3\Pi_g(\nu = 1)$ transition in N_2, where ν is the corresponding vibrational state) as a function of the filament length. The concept of forward and backward stimulated emission in the air is now known as air lasing. The atmosphere contains mainly oxygen and nitrogen with a bit of argon. Therefore, air lasing is very limited by its gain medium. Another limitation is that the lasing needs to be single pass (i.e., mirror-less); high gain is required as there is no resonator to amplify.

For air lasing to become a useful tool for remote sensing, it must be realized at large distances. This can be realized by exploiting the process of laser filamentation[3] which can be used to pump the air laser. Filamentation can be used to maintain high intensities over very large distances and can be initiated kilometers away from the target region. One type of lasing effect in an air filament is related to the molecular nitrogen ion (N_2^+), emitting primarily at 391 nm, 428 nm, and 471 nm wavelengths which is the focus of this thesis.

1.2 The N_2^+ lasing problem

The wavelengths corresponding to the N_2^+ lasing action corresponds to the $B^2\Sigma_u^+(\nu = 0, 1, 2)$ to $X^2\Sigma_g^+(\nu = 0, 1, 2)$ transitions where B is the excited state and X is the ground state as shown in Figure 1.1.

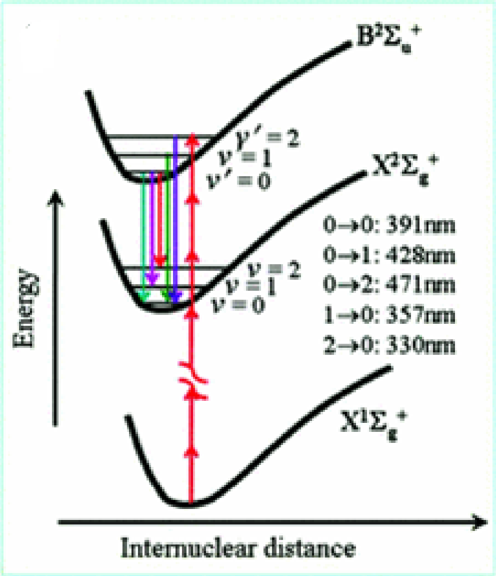

Figure 1.1: Energy-level diagram of ionized and neutral nitrogen molecules in which the transitions between $B^2\Sigma_u^+$ and $X^2\Sigma_g^+$ states are indicated with corresponding lasing wavelengths. Figure adapted from [1].

This lasing action was first observed in 2011 by J. Yao et *al.*[1]. These emissions were observed with femtosecond pump pulses in the UV, visible and mid-IR. Up to now, the physical mechanism underlying the lasing effect in N_2^+ is still subject to controversy. Some proposed mechanisms include the concept of natural population inversion, recollision excitation, multiple state coupling, and lasing without inversion. These potential mechanisms will be discussed in more details at the end of this thesis.

Backward lasing is a key concept for air lasing to become a useful tool for remote sensing. Backward lasing from the neutral molecular nitrogen has been previously experimentally demonstrated [1, 16, 17]. However backward stimulated emission from N_2^+ has yet to be achieved.

1.3 Thesis outline

I briefly introduced the concept of air lasing and its potential application in remote sensing. In my thesis, I start by introducing molecular energy levels and transitions as well as molecular alignment and rotational wavepackets. After which I introduce basic nonlinear optics and how filaments are formed and how they lead to air lasing. The first set of experiments that I present is done in filaments in ambient air. The rest of the thesis studies the N_2^+ lasing emissions in a supersonic gas jet in vacuum chambers. The sections are separated as follows.

Section two (Molecular dynamics): Section two introduces the energy levels of diatomic molecules and how transitions between energy levels can occur. I then briefly introduce frequency domain and time-domain spectroscopy. I finally discuss molecular alignment and how rotational wavepackets are created.

Section three (Nonlinear optics and filamentation): In section three, I briefly introduce nonlinear optics starting from Maxwell's equations and the Kerr effect. I follow the discussion with consequences of the Kerr effect such as self-focusing, self-phase modulation, self-steepening, and how, due to the balance between self-focusing and plasma defocusing due to ionization, filaments can be formed. In the second part of the section, I introduce properties of filamentation such as lasing from filaments.

Section four (N_2^+ lasing in filaments): In section four, I give a brief historical background on N_2^+ lasing in filaments and how recollision was proposed as a mechanism to create a population inversion in this system. The experimental part of this section reproduces previous results and are analyzed more closely by considering the filament initiated continuum behavior around the observed emission lines.

Section five (The role of recollision in N_2^+ air lasing): This section introduces a better way to study the gain by using a pump-probe scheme and focusing in a supersonic gas jet in a vacuum. We present solid evidence that recollision doesn't play a significant role in N_2^+ air lasing by comparing the ellipticity dependence of the gain with pump pulses with the ellipticity dependence of the generated high harmonics.

Section six (N_2^+ lasing in a thin gas jet): In this section, we use the same pump-probe method employed in section five to search for another potential gain mechanism. We do this by looking at the time evolution of the gain and by varying parameters such as pump intensity, jet position, and plasma density. We finally observe a second gain mechanism that would not be distinguishable in filaments.

Section seven (Discussion): In this section, I start by reviewing some of the properties of the N_2^+ emissions such as the build-up and decay time. The second part of the discussion reviews the proposed gain mechanisms from literature and how they link to our experimental observations.

2 Molecular dynamics

The air lasing gain medium consists of diatomic molecules such as O_2, N_2 and N_2^+; the later will be studied in this thesis. This section discusses the characteristics of such molecules. I start by introducing the vibrational and rotational energy levels that make molecules unique from simple atoms. After which possible transitions between energy levels are discussed and how spectroscopy can be done on emission and absorption lines. The end of this section introduces the concept of molecular alignment and how rotational wavepackets are created.

2.1 Energy levels of diatomic molecules

Molecules are made up of atoms that are held together by chemical bonds. These bonds allow the molecules to vibrate and rotate; giving them added energy levels in addition to the common electronic energy levels. For the purpose of this thesis, I will limit the discussion to simple diatomic molecules.

The vibration of diatomic molecules can be approximated by considering the chemical bonds between the atoms as a spring holding two balls together. The bond would have a spring constant k, and the molecule would have an effective mass μ with an angular frequency ω. Assuming the spring acts as a perfect harmonic oscillator, the energy levels are given by the quantum harmonic oscillator model:

$$E_\nu = \hbar\omega(\nu + \frac{1}{2}) \tag{2.1}$$

where ν= 0, 1, 2, ..., $\hbar = h/2\pi$, where h is the planck constant, and ω is given by:

$$\omega = \sqrt{\frac{k}{\mu}} \tag{2.2}$$

In the case of this perfect quantum harmonic oscillator, the energy difference between levels is calculated to be:

$$E_{\nu+1} - E_{\nu} = \hbar\omega \tag{2.3}$$

Note that we have assumed a harmonic oscillator with a quadratic potential function. In reality, the oscillator of the molecule is anharmonic, and the potential function needs to be approximated using, for example, a Morse potential.

On the other hand, to consider molecular rotations, it suffices to approximate the molecule as a rigid rotor. The rigid rotor model is well known and has quantized energy levels given by

$$E_J = \frac{\hbar^2}{2I} J(J+1) \tag{2.4}$$

where J = 0, 1, 2, ... is the angular momentum and I is the moment of inertia and is given by $I = \mu r^2$ where μ is the reduced mass and r the bond length of the molecule. It is more common to write this as [18]

$$E_J = hcBJ(J+1) \tag{2.5}$$

where B is referred to as the rotational constant of the molecule and is given by:

$$B = \frac{\hbar}{4\pi c I} \tag{2.6}$$

The energy difference between each adjacent rotational energy level is calculated to be:

$$E_{J+1} - E_J = 2hcBJ \tag{2.7}$$

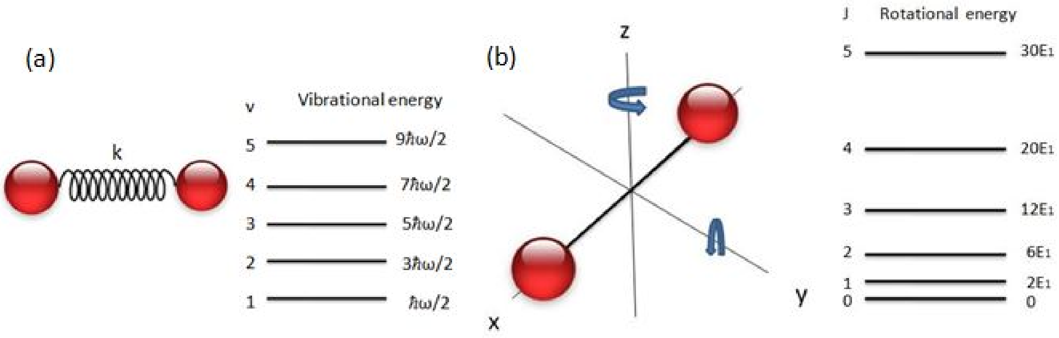

Figure 2.1: (a) Schematic representation of a ball on a spring with associated quantized energy levels. (b) Schematic representation of the rigid rotor with associated quantized energy levels where $E_1 = hcB$. The spacing between energy levels is not to scale.

It is important to note that the energy spacing between rotational levels is much smaller than vibrational levels. In fact, each vibrational level has rotational bands built on it.

The energy levels of molecules are therefore the sum of its rotational, vibrational and electronic energy levels (E_n). i.e.,

$$E_{molecule} = E_J + E_\nu + E_n \tag{2.8}$$

Figure 2.2 shows a crude approximation but realistic energy diagram of two different electronic states in a molecule.

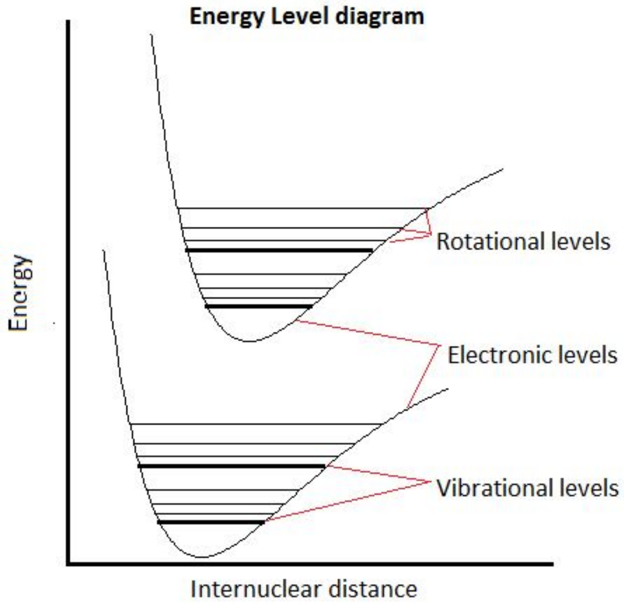

Figure 2.2: Approximate energy diagram showing electronic, vibrational and rotational energy levels of a molecule.

2.2 Molecular transitions

Transitions between molecular energy levels are possible through several processes. A molecule can be raised from a lower energy state to a higher state by absorption of energy such as absorption of photons. The energy absorbed must be in resonance with an energy spacing between two states. A molecule in an excited state will eventually undergo a process known as spontaneous emission where the molecule goes from a higher energy state to a lower one, emitting a photon of energy equal to the energy spacing of the levels involved. The emitted photons from this process is known as fluorescence. Such reduction of energy level can also be stimulated by another photon. The emitted photon is an exact replica of the photon that induced the process. Finally, a molecule can decrease in energy level by nonradiative deexcitation. The emitted energy appears in another form such as increased vibrational or rotational levels.

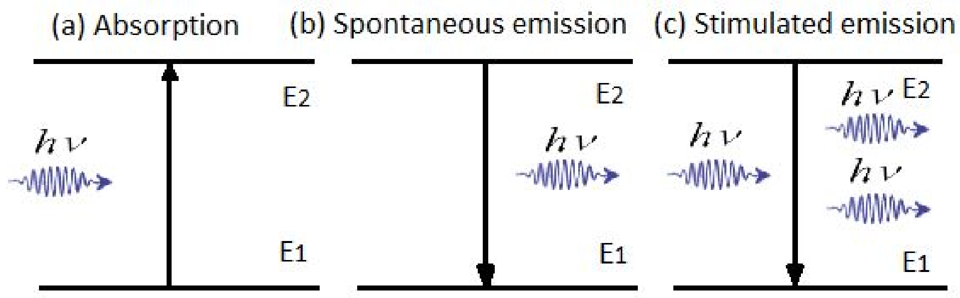

Figure 2.3: Absorption and emission processes in atoms and molecules. E1 is the lower energy state and E2 is the higher energy state.

2.2.1 Transition moment

When an atom or molecule absorbs a photon, there's a probability the atom or molecule will transit from one energy state to another. It depends on two things: the nature of the states wavefunctions and how strongly photons interact with an eigenstate. Transition strengths are used to describe such transition probability.

An electromagnetic wave can induce an oscillating electric or magnetic moment in an atom or molecule. The transition moment is the electric dipole moment associated with the transition between two states. It is the probability of a molecule to transition from one state to another. It can be written in mathematical form as

$$\mu_{fi} =< \psi_f|\mu|\psi_i >$$

where ψ_f denotes the final state,ψ_i the initial state and $\mu = -er$ is the electric dipole operator. Transitions for which $\mu_{fi} \neq 0$ are known as allowed transitions, while those for which $\mu_{fi} = 0$ are known as forbidden transitions. Selection rules discussed in the next section are utilized to know if a transition is allowed or not.

Oscillator strength is a measure often used to describe the strength of a transition and is given as a function of the square of the dipole moment [19]

$$f = \frac{8\pi^2 m_e \nu_{fi}}{3e^2 h} |\mu_{fi}|^2 \tag{2.9}$$

where m_e is the electron mass, ν_{fi} is the frequency associated with the transition, and e is the electron charge.

Selection rules have been divided into electronic selection rules, vibrational selection rules, and rotational selection rules.

2.2.2 Selection rules

An electronic state is typically represented as

$$\Omega^{2S+1}\Lambda^{(+/-)}_{(g/u)}$$

where S is the spin quantum number, Λ is the angular momentum quantum number, g/u is the parity, and +/- is the reflection symmetry. $\Lambda = 0$, 1, 2, 3 are represented by the symbols Σ, Π, Δ, and Φ respectively. Ω represents the actual electronic state. The letter X is reserved for an electronic ground state while the first excited state is defined as A, the second B, and so on.

The electronic selection rules for molecules are as follows [20, 21]; The total spin can't change (i.e., $\Delta S = 0$), The angular momentum can only change by $\Delta\Lambda = 0, \pm 1$, and $g \Leftrightarrow u$ transitions are allowed for homonuclear molecules while $+ \Leftrightarrow +$ and$- \Leftrightarrow -$ transitions apply for heteronuclear molecules.

On the other hand, vibrational selection rules are simple. Transitions with $\Delta\nu = \pm 1, \pm 2, ...$ are all allowed, and $\Delta\nu = 0$ transitions are allowed between electronic states.

Finally, rotational selection rules are simply $\Delta J = 0, \pm 1$. This is due to the conservation of angular momentum. This selection rule applies because photons have one unit of angular momentum and the total angular momentum needs to be conserved. Furthermore, $\Delta J = 0$ can only occur when there's a net orbital angular momentum in one of the electronic states.

Transitions with $\Delta J = 1$ are defined as R branch transitions, while those with $\Delta J = -1$ are defined as P branch transitions, and $\Delta J = 0$ are defined as Q branch transitions. Rotational transitions are allowed to occur within electronic states or between electronic states. The Q branch is therefore not allowed in the N_2^+ $B^2\Sigma_u^+ \rightarrow X^2\Sigma_g^+$ transitions that will be studied in this thesis because the electronic levels have no orbital angular momentum.

2.3 Spectroscopy

Rotational and vibrational transitions of molecules help us identify how molecules interact with each other and their bond length. To know each transition, we have to consider other terms like wave number, force constant, quantum number, etc. There are rotational energy levels associated with all vibrational levels. From this, vibrational transitions can couple with rotational transitions to give rovibrational spectra. Rovibrational spectra are often used to determine the average bond length of molecules, for example.

2.3.1 Frequency domain spectroscopy

Most spectroscopy to date has been performed in the frequency domain (i.e., as a function of frequency or wavelength). This type of spectroscopy can be used to determine molecular structures and properties. In a spectroscopic experiment, light is passed through a sample, and the sample can absorb some wavelengths. A given molecule will only absorb photons whose energy has the same energy that corresponds to a specific transition. By observing which wavelengths were absorbed and how much was absorbed, information about the molecule can be obtained.

2.3.2 Time-domain spectroscopy

Time-domain spectroscopy is another type of spectroscopy that can measure the intensity of electromagnetic radiation as a function of time. The famous pump-probe spectroscopy method can be employed to examine molecular dynamics. A first pulse will initiate particular dynamical behavior in a molecule and, at a time delay later, a second weak probe would yield a spectrum from which instantaneous molecular structures can be observed. However, molecular dynamics occur at times shorter than 10^{-10} s for molecular vibrations and 10^{-13} s for molecular rotations[22, 23]. Therefore the method has been limited until the femtosecond laser came into existence in the 1980s[24][25]. By varying the delay between the pump and probe pulses, the time evolution of the molecule can be observed. Femtochemistry was then developed, and a Nobel prize was awarded to A. Zewail in 1999 for the development of the field of femtochemistry[26, 23]. More recently, attosecond pulses as short as 53 attoseconds can be generated[27] through high harmonic generation and can be used to probe the dynamics of electrons which orbit the nucleus on a timescale of attoseconds. Time-domain spectroscopy usually requires the use of the Fourier transform to analyze time-domain spectra in the frequency domain. The majority of the work that will be presented in this thesis study the dynamics of N_2^+ by the use of time-domain spectroscopy.

2.4 Molecular alignment

Under no external influences, molecules would be rotating in random orientations. Therefore, molecules will naturally not be aligned with each other. However molecular alignment is possible for non-spherically symmetric molecules. There are numerous applications to achieve molecular alignments such as material processing and laser-molecule interaction. The process of molecular alignment has been widely studied due to its crucial role in chemistry and physics, and different techniques to align molecules have been developed.

The first approach was with the use of a static electric field [28]. This relies on molecules having the need of a permanent dipole moment to align the molecules. Using a strong electric field, such as the one created by an intense laser beam, one can induce a dipole moment on molecules, and therefore, overcoming the restriction from using a static electric field. Friedrich and Hershbach treated molecular alignment theoretically using laser pulses [29, 30]. However, the laser pulses were much longer than the rotational period of the molecule. In this case, the molecules become aligned in the presence of the laser pulse and return to an isotropic state after the laser pulse. This process is called adiabatic alignment, and its first demonstration was in 1996 [31].

If the laser pulse is shorter than the rotational period of the molecules, the molecules cannot adiabatically adapt to the laser field, resulting in a time-dependent “field-free alignment”. This was first treated theoretically by Seideman[32] and experimentally shown by Rosca-Pruna [33]. The laser pulse 'kicks' the molecules towards alignment, but the pulse passes through the system before the molecules has time to align. However, shortly after, the molecules will become aligned with each other. In this regime, during the alignment of the molecules, there are no fields present which can distort molecules. This is what is known as field-free alignment. The result can be described as a coherent superposition of rotational states, known as a rotational wavepacket.

2.4.1 Rotational wavepackets

Looking at the time evolution of a rotational wavepacket is interesting. Considering a diatomic molecule such as N_2 that can be approximated by a rigid rotor, the rotational wavepacket behavior is simple. The rotational frequencies ω_J are given by Equation 2.5 with $E_J = \hbar\omega_J$. There is, therefore, a fundamental period (for $J = 0$) given by

$$T_{rev} = \frac{1}{2Bc} \tag{2.10}$$

where T_{rev} is known as the revival period of the molecule. Since J is an integer, the only possible rotational frequencies must be multiples of the fundamental. Therefore, every T_{rev}, the rotational wavepacket will re-phase (i.e., revive) itself to any T_{rev} state before. For example, N_2 has a rotational constant of 1.998 and Equation 2.10 yields a revival time of 8.34 ps. Figure 2.4 shows the revival structure of N_2 molecules.

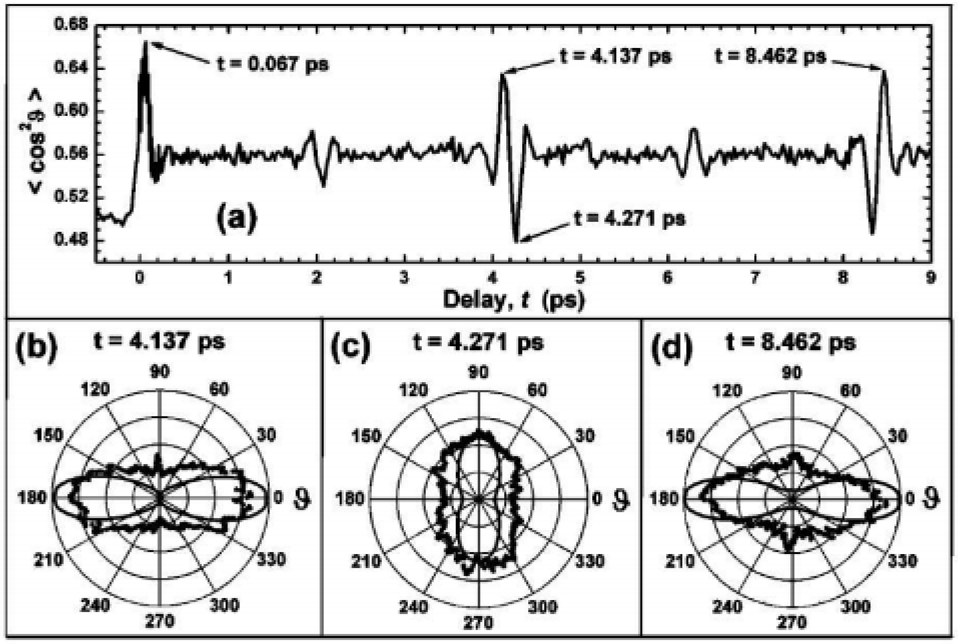

Figure 2.4: (a) Experimentally measured alignment revival structure for N2. (b) - (d) Plots of measured (thick) and simulated (thin) angular distributions for select times along the revival structure. Courtesy of Ref. [2].

During times of revivals, the molecules go from alignment to anti-alignment. Anti-alignment is referred to an alignment perpendicular to the aligning field as in Figure 2.4 (c). Fractional revivals also occur at $T_{rev}/4$, $T_{rev}/2$, and $3T_{rev}/4$ but I do not attempt to explain them in this thesis.

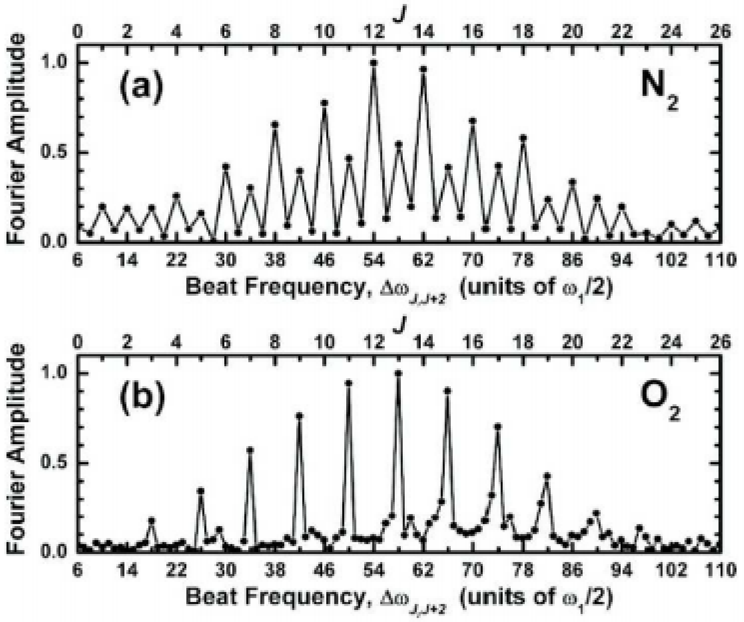

Figure 2.5: Fourier transform of (a) N_2 and (b) O_2 showing the retrieval of rotational J states from the time domain rotational wavepacket. Courtesy of Ref. [2].

Figure 2.5 shows the use of the Fourier transform on a rotational wavepacket. J states can be retrieved from this method, which are sometimes not shown by starting with analysis in the frequency domain.

3 Nonlinear optics and filamentation

3.1 nonlinear optics

3.1.1 Maxwell's equations

Electromagnetic waves in a medium propagate following Maxwell's equations. If there is no magnetic field present in the medium, Maxwell's equations are [34]:

$$\nabla \cdot \boldsymbol{D} = \rho \tag{3.1}$$

$$\nabla \cdot \boldsymbol{B} = 0 \tag{3.2}$$

$$\nabla \times \boldsymbol{E} = -\frac{\partial \boldsymbol{B}}{\partial t} \tag{3.3}$$

$$\nabla \times \boldsymbol{B} = \mu_0 \frac{\partial \boldsymbol{D}}{\partial t} + \mu_o \boldsymbol{J} \tag{3.4}$$

where $\boldsymbol{E}$ is the electric field, $\boldsymbol{D}$ is the electric displacement field, $\boldsymbol{B}$ the magnetic field, and μ_0 is the vacuum permeability. The electric displacement field and the electric field is related by $\boldsymbol{D} = \epsilon_0 \boldsymbol{E} + \boldsymbol{P}$, where $\boldsymbol{P}$ is the polarization of the medium and ϵ_0 is the permittivity of vacuum. Introducing a factor known as susceptibility we can rewrite this relationship as $\boldsymbol{D} = \epsilon_0(1+\chi)\boldsymbol{E} = \epsilon_r \epsilon_0 \boldsymbol{E}$ and $\boldsymbol{P} = \epsilon_0 \chi \boldsymbol{E}$. We can express the polarization $\boldsymbol{P}$ as a power series as

$$\boldsymbol{P}(t) = \epsilon_0[\chi^{(1)}\boldsymbol{E}(t) + \chi^{(2)}\boldsymbol{E}^{\boldsymbol{2}}(t) + \chi^{(3)}\boldsymbol{E}^{\boldsymbol{3}}(t) + \cdots] \tag{3.5}$$

where $\chi^{(1)}$ is known as the linear optical susceptibility and $\chi^{(2)}$ and $\chi^{(3)}$ are known as the second and third order nonlinear optical susceptibility.

3.1.2 Nonlinear refractive index

Due to inversion symmetry, which is the case for gases, the even order terms vanish, and therefore, we may write

$$\boldsymbol{P}(t) = \epsilon_0[\chi^{(1)}\boldsymbol{E}(t) + \chi^{(3)}\boldsymbol{E}^{\mathbf{3}}(t) + \cdots] \tag{3.6}$$

By omitting the terms $\chi^{(5)}$ and greater and by combining Maxwell's equations, the optical wave equation in nonlinear optics is obtained [34]:

$$\nabla \times \nabla \times \boldsymbol{E}(t) - \frac{1}{c^2}\frac{\partial^2 \boldsymbol{E}(t)}{\partial^2 t} = -\mu_0 \frac{\partial^2 \boldsymbol{P}(t)}{\partial^2 t} \tag{3.7}$$

The refractive index is then determined as a function of intensity I of the field:

$$n = n_0 + n_2 I(r, t) \tag{3.8}$$

Where the intensity I(r,t) is

$$I = 2n_0\epsilon_0 c|E(r, t)|^2 \tag{3.9}$$

and the nonlinear refractive index is

$$n_2 = \frac{3}{4n_0^2\epsilon_0 c}\chi^{(3)} \tag{3.10}$$

where n_2 is known as the Kerr term. Since the coefficient n_2 is positive in most materials, the total refractive index will increase with increasing intensity. n_2 for gases is typically around the order of 10^{-19} cm^2/W at a pressure of 1 bar. At intensities normally encountered in linear optics, only the first term in equation 3.8 is significant, and the refractive index can be considered a constant (n_0).

3.1.3 Self-focusing

The optical Kerr self-focusing effect was predicted in the 1960s[35, 36, 37] and experimentally verified in glasses and liquids[38, 39]. As seen in Equation 3.8, if an electromagnetic field has a high enough intensity so that the nonlinear intensity-dependent term becomes significant, then the refractive index will be modified. For example, a beam with a Gaussian spatial profile will see a higher refractive index at the center of the beam than the outside. As a result, a phase difference between the central and the outside parts of the pulse is induced during propagation. The refractive index difference will then act as a positive lens, thus focusing the beam as shown in Figure 3.1.

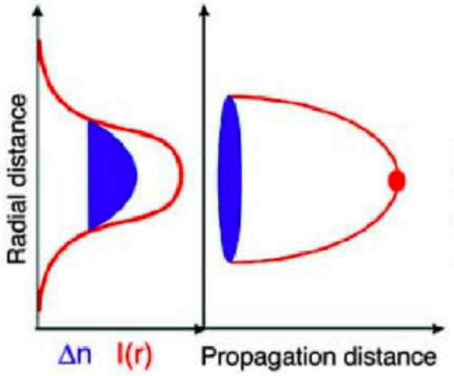

Figure 3.1: Self-focusing of a laser beam by the optical Kerr effect. Figure adapted from [3].

A parameter that is important for self-focusing to occur is the initial power of the laser beam. A beam will only self-focus if it overcomes diffraction limits which is a threshold called the critical power (Pcr) and is given by:

$$Pcr = \frac{3.77\lambda_0^2}{8\pi n_0 n_2} \tag{3.11}$$

This can be derived by equating the diffraction effect with the self-focusing effect. i.e.,

$$\theta_{dif} = \theta_{sf} \tag{3.12}$$

where θ_{dif} is the diffraction effect can be approximated by

$$\theta_{dif} = \frac{a\lambda_0}{n_0 d} \tag{3.13}$$

where a is a constant which depends on the beam in question (a is 0.61 for a Gaussian beam) [34] and d is the beam FWHM diameter. θ_{sf} is the self-focusing effect given by [34]

$$\theta_{sf} = \sqrt{\frac{2n_2 I}{n_0}} \tag{3.14}$$

where I is the peak intensity. We then get:

$$I = \frac{a^2\lambda_0^2}{2n_2 n_0 d^2} \tag{3.15}$$

The peak power contained in the laser beam is:

$$P = \frac{\pi}{4} d^2 I \tag{3.16}$$

We then get the result in Equation 3.11 up to a proportionality constant. For a near-infrared pulse with 42 fs pulse duration, the critical power is measured to be about 10 GW [40]. It is important to note that we have assumed a Gaussian beam to get the coefficient in Equation 3.11. For example, the coefficient 3.77 must be replaced by 3.72 for a Townes beam[3].

We can approximate the propagation length of the self-focusing beam until collapse by the semi-empirical formula of Dawes and Marburger[41, 42]

$$L_c = \frac{0.367 L_{DF}}{\sqrt{[(P_{in}/P_{cr})^{1/2} - 0.852]^2 - 0.0219}} \tag{3.17}$$

where $L_{DF} = \pi\omega_0^2/\lambda_0$ is the Rayleigh length, which is the characteristic length of diffraction of a Gaussian beam, P_{in} is the input power, and ω_0 is the beam waist.

If we start with a collimated beam with a wavelength of 800 nm, with power $P_{in} = 10P_{cr}$ and a beam waist of 50 mm, the distance before collapse is ~15.6 m. However, equation 3.17 breaks down at higher input powers due to modulational instabilities[43].

In a laboratory experiment, it is most practical to aid the self-focusing effect by focusing the collimated beam with a lens. The position of collapse, therefore, moves before the position of the focus of the lens according to [44]

$$\frac{1}{L_{c,f}} = \frac{1}{L_c} + \frac{1}{f} \tag{3.18}$$

where f is the focal length of the lens.

3.1.4 Self-phase modulation

Due to the nonlinearity of the refractive index of a medium, a pulse's phase can be self-modulated during propagation which is known as self-phase modulation (SPM). This nonlinearity originates from the Kerr effect and describes the response of a material refractive index to the applied field (see Equation 3.8). The total phase of a Gaussian pulse is

$$\phi(t) = w_0 t - nkL \tag{3.19}$$

where $k = 2\pi/\lambda$ is the wavenumber, ω_0 is the carrier frequency, and L is the propagation length. Due to the nonlinear refractive index, a time-dependent phase arises. The effect of the medium is to change the phase of the pulse by:

$$\phi_{NL} = -n_2 IkL = -n_2 I(t)\omega_0 L/c \tag{3.20}$$

The instantaneous frequency of the pulse ω_{inst} is given by the time derivative of the total phase:

$$\omega_{inst}(t) = \frac{d}{dt}(\omega_0 t + \phi(t)) = \omega_0 + \frac{d}{dt}\phi_{NL}(t) \tag{3.21}$$

The variation of ω_{inst} is called chirp. Assuming a positive n_2 constant, the frequency is down-shifted at the leading edge of the pulse. Whereas, the frequency is up-shifted at the trailing edge. In other words, the leading edge is red-shifted and effectively travels faster than the blue-shifted trailing edge.

The dimensionless B parameter, also known as the B-integral

$$B = \frac{2\pi}{\lambda}\int n_{2I} I dz \tag{3.22}$$

is often used to measure the strength of the nonlinear effect due to the Kerr nonlinear refractive index. Values of $B > 1$ usually results in significant nonlinear effects, including self-focusing and SPM. SPM plays a dominating role in the generation of supercontinuum covering a large wavelength range.

3.1.5 Self-steepening

Another nonlinear effect that arises from the Kerr effect is Self-steepening. This effect arises from the intensity dependence of the group velocity. The velocity of the peak intensity of the pulse is smaller than that of its wings. Therefore the back of the pulse will catch up to its peak[45]; a shock front is formed in correspondence of this edge, and self-steepening brings an increase in the generation of bluer frequency. In condensed media, the formation of a leading shock front has been observed and investigated[46].

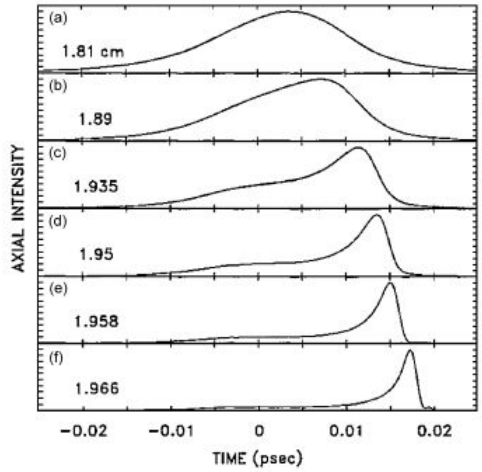

Figure 3.2: Calculated intensity as a function of time of a self-focusing and self-steepening pulse in a normal dispersive medium. The propagation distances are indicated on the graphs in cm. Courtesy of Refs. [4, 3].

3.1.6 Multiphoton ionization and plasma defocusing

Self-focusing will eventually lead to ionization of the medium in question. Another nonlinear effect that will occur is multiphoton ionization. Multiphoton ionization is the simultaneous absorption of multiple photons that eventually lead to ionization. The number of photons required to ionize is approximately $K = I_p/\hbar\omega$ which is approximately 10 photons to ionize N_2 with 800 nm photons and I_p is the ionization potential. Peak laser intensities above 10^{12} W/cm^2 are typically required for such process to occur. A plasma is created as a result and provides a negative change to the refractive index. This will act against the self-focusing effect and defocus the laser pulse.. The reduction follows the law[47, 3]

$$n \simeq n_0 - \frac{\rho(r,t)}{2\rho_c} \tag{3.23}$$

where $\rho(r,t)$ is the density of free electrons, and $\rho_c = \epsilon_0 m_e \omega_0^2/e^2$ is the value of the critical plasma density. Above this value the plasma becomes opaque[3].

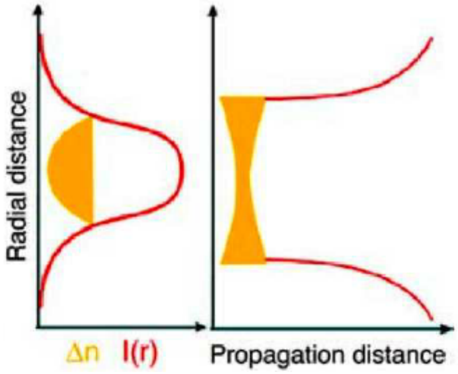

Figure 3.3: Defocusing of a laser beam by the presence of a plasma. Figure adapted from [3].

3.1.7 Formation of filaments

The combined action of self-focusing of a laser pulse due to the optical Kerr effect and the defocusing of the pulse due to plasma defocusing results in multiple cycles of focusing-defocusing, and therefore, the creation of light filaments. This process is shown in Figure 3.5.

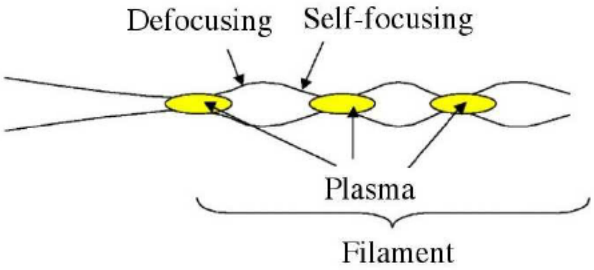

Figure 3.4: Filamentation schematic representation of the focusing-defocusing cycles. The filamentation length is the distance covered by these cycles. Courtesy of Ref. [3].

The defocusing beam will self-focus until the remaining power of the defocusing beam drops below the critical power for self-focusing.

3.2 Properties of filamentation

3.2.1 Intensity clamping

Due to plasma defocusing, an intense laser pulse can only focus to a certain intensity before defocusing dominates. This means that the intensity in a filament is clamped. This clamped intensity can be approximated by[48, 49, 50]

$$I \sim (\frac{2n_2\rho_c}{\sigma_K t_p \rho_{at}})^{K-1} \tag{3.24}$$

where ρ_{at} denotes the density of neutral atoms, K the number of photons and σ_K is the ionization cross section.This yields a clamped intensity of 1.8×10^{13} W/cm^2 for a pulse duration of $t_p = 100$ fs at 800 nm [3]. In air, for 800 nm laser pulses, the clamped intensity seems to be actually around $I = 5 \times 10^{13}$ W/cm^2 [49, 50]. However, newer studies shows that intensity in a filament can go as high as 1.45×10^{14} W/cm^2[51].

Intensity clamping has an incredible advantage for atmospheric studies. In an non filamentation regime, diffraction limits the intensity that can be achieved at a focus point. If we assume a Gaussian beam, the beam diameter will linearly increase with focusing distance following

$$\delta\phi = \frac{2f\lambda}{\pi D} \tag{3.25}$$

For a fixed laser power the focal intensity decreases following the relation $1/f^2$. On the other hand, the clamped intensity of a filament provides non diffraction limited ionization zone of near constant uniform intensity throughout the filament zone. This is independent of focusing distance and pulse width/energy.

3.2.2 Long range propagation

One of the reasons why filamentation is such an interesting phenomena is its ability to propagate high intensities over extended distances. Peak intensities above 10^{12} W/cm^2 have been observed over several kilometers via filamentation[52].

3.2.3 Spectral broadening

Filamentation is a highly nonlinear system that allows the generation of new frequencies. Filamentation strongly broadens the pulse through self-phase modulation, ionization, and self-steepening[3]. This effect is commonly known as suppercontinuum generation (or just continuum) or white light generation. Filaments have been shown to generate ultra-broad spectra that can extend from the infrared to the visible. Figure 3.5 shows a continuum generated from propagation over 10 m in air. This effect will be utilized in this thesis to seed the emissions from N_2^+ in filaments.

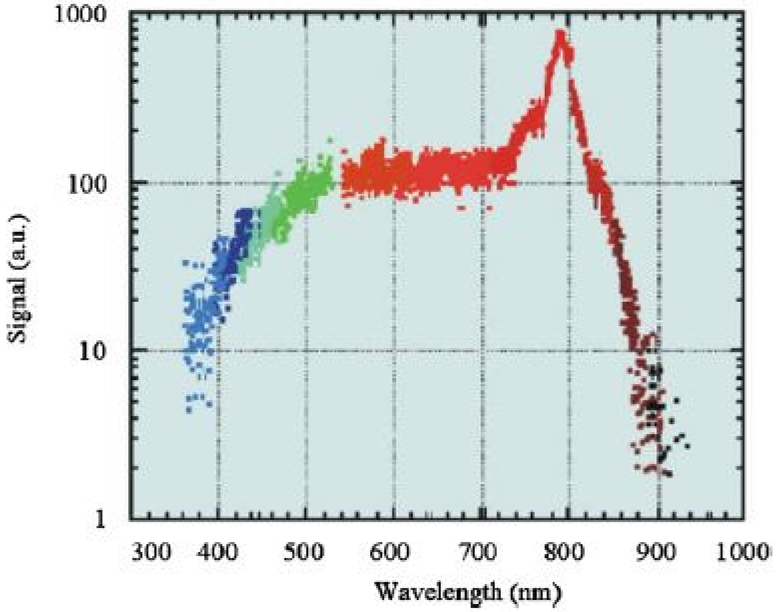

Figure 3.5: Spectrum of a 800 nm laser beam, with FWHM of 70 fs, and a peak power of 3 TW after propagation over a distance of 10 m in air. Courtesy of Ref. [3].

3.2.4 Conical emission

Conical emission is one of the most noticeable properties of filamentation and is caused by supercontinuum generation. The main signature of conical emission is that the redder frequencies appear at the center of the emission while the bluer components appear on the outside, which is the inverse of what you would expect from diffraction. This phenomenon is not entirely understood, but some mechanisms have been proposed such as Cerenkov radiation [53, 54], X-waves [55, 56, 57], self-phase modulation [58], and four-wave mixing [59, 60]. Figure 3.7 (a) shows the typical conical emission from a 1mm long filament.

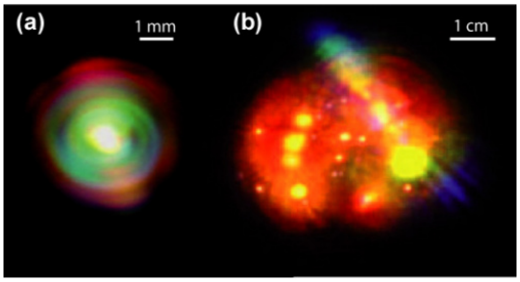

Figure 3.6: (a) Conical emission from a 1mm long filament observed on a screen; (b) Multifilament pattern on a screen from a 1 cm long filament. Note: The figure does not show real colors. Courtesy of Ref. [5]

However, Figure 3.6(b) highlights how messy the process of filamentation is as the filament length is increased.

3.2.5 Filamentation and molecular alignment

As seen in Section 2.4, the femtosecond laser pulses that create the process of filamentation also give an instantaneous quantum "kick" to the molecules, which creates what is known as a wavepacket. The wavepacket shows field-free revival structures. This alignment process in filaments is one of many potentially important applications of filamentation.

3.2.6 Filament induced lasing action

Not only does self focusing increase the intensity of a laser pulse and eventually ionize a medium, the laser also excites molecules and ions into excited states. These excited states can then emit fluorescence [61, 62]. An exponential increase in intensity of this florescence in the forward and backwards direction has been detected with increasing filament length. This process is known as amplified spontaneous emission (ASE) lasing. N_2 and N_2^+ emissions in air filaments are such examples, although backwards lasing from N_2^+ has yet to be reported. Filament induced lasing is potentially very important for remote sensing applications. Gain in N_2^+ is the focus of my thesis.

4 N_2^+ Lasing in filaments

4.1 Historical background

In 2011, J. Yao et *al.* reported strong stimulated emission lines in the forward direction in ambient air and pure nitrogen [1]. The radiation lines at 330 nm, 357 nm, 391 nm, 428 nm, and 471 nm wavelengths were activated using a wavelength tunable near-IR laser ($1.2\mu m$ - $1.9\ \mu m$) as shown in Figure 4.1. The effect corresponds to the $B^2\Sigma_u^+$ to $X^2\Sigma_g^+$ transition between the excited and ground state of the nitrogen molecular ion. They found that when the spectrum of the 3rd or 5th harmonic of the driving pulse covered these lines, N_2^+ emissions can be initiated. This amplification effect was attributed to the realization of population inversion that occurs at an ultrafast time scale. They attributed the population inversion mechanism to the direct formation of excited molecular nitrogen ions by strong-field ionization of inner-valence electrons. Although the used seeding wavelengths covered some emission lines of pure molecular nitrogen, no such emission was detected.

In 2013, Andriukaitis et *al.* observed the forward 391 nm and 428 nm lasing emission by focusing millijoule pulses at 1.03 μm femtosecond pulses in a gas cell filled with nitrogen[63]. They attempt to explain the emission to four-wave mixing between the intense near-IR pulses and weak supercontinuum components in resonance to the transitions.

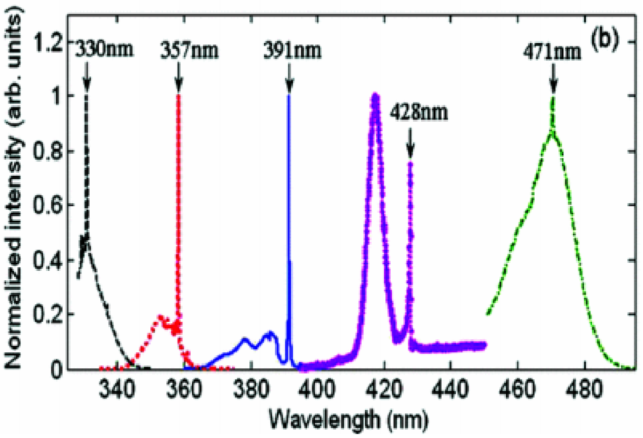

Figure 4.1: The lasing peaks at 471, 428, 391, 357, and 330 nm achieved with different pump wavelengths of 1415, 2050, 1920, 1760, and 1682 nm, respectively. Courtesy of Ref. [1].

Also in 2013, lasing at the 391 nm and 428 nm wavelengths was reported using a 800 nm femtosecond pump pulse followed by a seed pulse covering the wavelength of 391 nm and 428 nm[64, 65]. By manipulating the propagation direction, spectral property, and intensity of the probe, they concluded that the coherent emissions results neither from the parametric process of wave-mixing nor from stimulated Raman scattering. They also monitored the gain as a function of pump-seed delay where the duration of the emissions were shown to be a few picoseconds.

Then, by using an 800 nm femtosecond laser pulse, Liu et *al.* achieved lasing emission of N_2^+ from filamentation alone[66]. This was attributed to a self-seeding effect meaning that the continuum generated by the filament during propagation acts as the seed to amplify. Two other works also reported this self-seeding effect[67, 68].

Later on, pumping ambient air with 1.5 TW, 800 nm femtosecond laser pulses Point et *al.* observed forward emission at 428 nm with pulse energy of 2.6

μJ corresponding to an optical gain of 0.7/cm[69].

One proposed mechanism that has been brought forward is electron recollision excitation[6]. The authors arrived at this conclusion by comparing the High-Harmonic Generation (HHG) yield with the 391 nm and 428 nm emission lines and their behavior as a function of ellipticity of the excitation pulse.

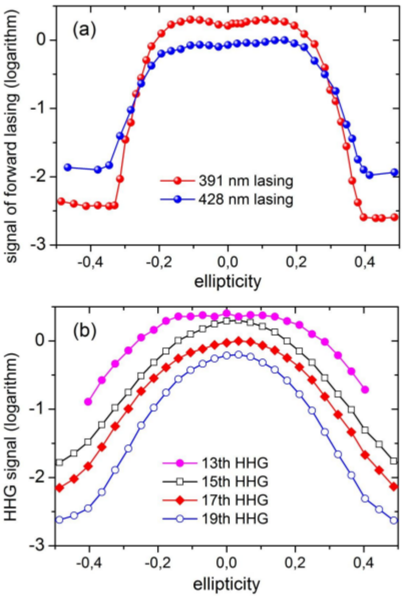

Figure 4.2: (a) 391 nm and 428 nm emission as a function of ellipticity of the 800 nm pump pulses measured in a gas cell at 45 mbar and 300 mbar nitrogen gas pressure, respectively. (b) High-order harmonic yield as a function of laser ellipticity. Courtesy of Ref. [6].

However, the gain seems to have an increase yield with ellipticity, which is not usually the case for HHG. For recollision to play a significant role we would expect only a decrease with ellipticity as the elliptical light will push the electrons away from the nucleus, providing a decrease in probability of recollision for any increase in ellipticity.

4.2 The experiment

To search for more experimental evidence that recollision plays a role in establishing a population inversion between the $B^2\Sigma_u^+$ and $X^2\Sigma_g^+$ states of N_2^+, we add ellipticity to the pump laser pulse. Adding ellipticity to the generating laser pulse decreases the probability of an electron recolliding with its parent ion, thus reducing the high harmonics yield and therefore the contribution of recollision to the gain in N_2^+. We start by measuring the ellipticity dependence of the gain in an air filament to expand on previous experiments [51, 67, 6, 70] as well as study the effect of the pump pulse duration.

4.2.1 Experimental setup

In order to study the ellipticity of the gain in N_2^+, we focus femtosecond laser pulses in ambient air to create a plasma channel. The laser system consists of a commercial Ti:Sapphire laser system (Legend Elite Duo, Coherent, Inc.) that provide 1 kHz, ~25 fs, and ~3.3 mJ train of pulses centered at 800 nm. A quarter-wave plate is used to control the ellipticity of the laser beam, while a polarizer is used to measure the polarization state of the beam and the transmitted light is collected in a fiber and analyzed by a spectrometer (Ocean Optics USB4000). The experimental setup that is shown in Figure 4.3 (a) is used to calibrate the polarization of the unfocused laser beam. Figure 4.3 (b) shows the typical spectrum of our laser pulses.

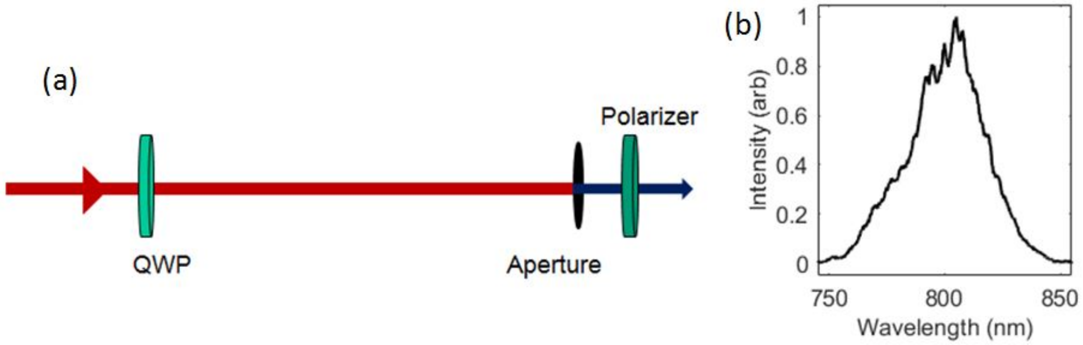

Figure 4.3: (a) Experimental setup for the calibration. (b) Spectrum of the laser pulses.

The calibration is performed by scanning each polarizer angle for every quarter-wave plate angle. A measurement of the calibration of the unfocused beam is presented in Figure 4.4 (a). The major axis of the elliptical light is shown as a function of quarter-wave plate angle in Figure 4.4 (b). The resulting ellipticity as a function of quarter-wave plate angle is shown in Figure 4.4 (c).

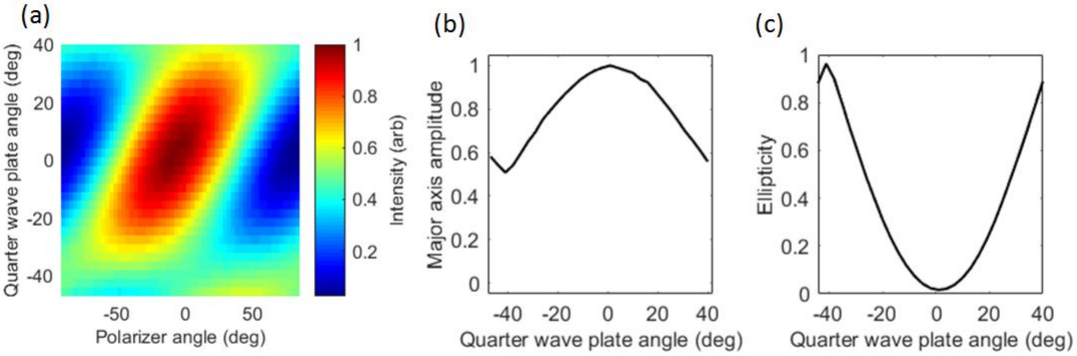

Figure 4.4: (a) Normalized transmission intensity (color scale) of the unfocused 800 nm beam as a function of quarter wave plate (QWP) and polarizer angle in degrees. (b) Intensity of the major axis of the elliptical beam as a function of the QWP angle in degrees. (c) Ellipticity as a function of QWP angle in degrees.

We then inserted different focusing lenses (30 cm, 40 cm, and 100 cm) after the quarter-wave plate to create a filament in ambient air to modulate plasma length and formation[71]. The on-axis emitted light from the plasma channel travels through an aperture and a polarizer and the transmitted light is then analyzed with a fiber spectrometer (Ocean Optics Maya2000 Pro) as shown in Figure 4.5 (a). A continuum is generated from the dynamics within the filament and acts as a seed to be amplified (self-seeding). We observe self-seeding emissions from the $B^2\Sigma_u^+$ to $X^2\Sigma_g^+$ states of N_2^+ emitting at 391 nm ($\nu' = 0 \rightarrow \nu = 0$), 428 nm ($\nu = 0' \rightarrow \nu = 1$), and 471 nm ($\nu' = 0 \rightarrow \nu = 2$) where ν' and ν are the vibrational state of the $B^2\Sigma_u^+$ and $X^2\Sigma_g^+$ states respectively. Figure 4.5 (b) shows the strong amplification of molecular ionic nitrogen at 428 nm which is the emission line that will be studied in this section.

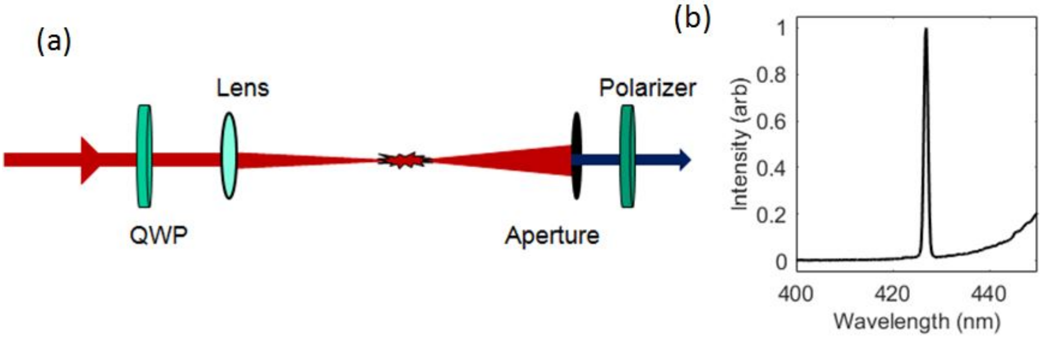

Figure 4.5: (a) Experimental diagram of gain measurement in air. (b) Typical transmission spectrum with amplification at 428 nm.

4.2.2 Experimental results

The same method used for the ellipticity calibration was used to analyze the transmitted 428 nm light. Every angle of the polarizer is scanned for every quarter-wave plate angle. The raw data, using a 30 cm focusing lens, is presented in Figure 4.6 (a). The major axis amplitude is plotted as a function of quarter-wave plate angle in Figure 4.6 (b), and the ellipticity is presented in Figure 4.6 (c) as a function of quarter-wave plate angle.

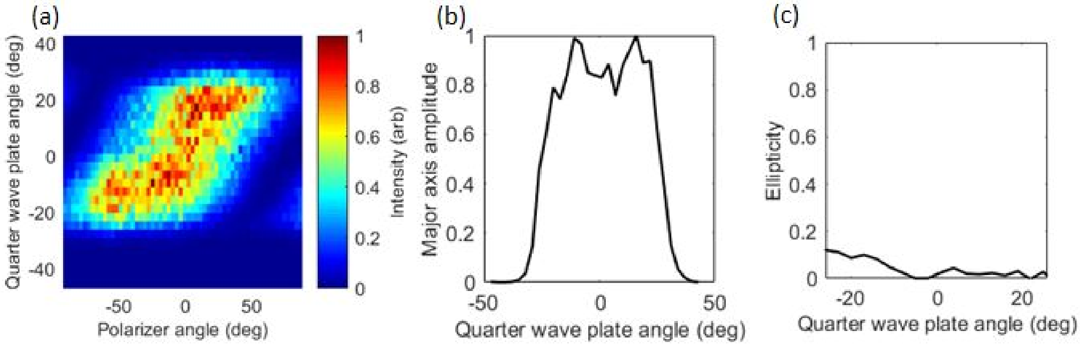

Figure 4.6: (a) Intensity of the 428 nm emission (colour scale) from the air filament as a function of QWP and polarizer angle in degrees. (b) Intensity of the major axis of the elliptical beam as a function of the QWP angle in degrees. (c) Ellipticity as a function of QWP angle in degrees.

Figure 4.6 (b) shows a clear nonzero enhancement with quarter-wave plate angle, showing a similar behavior as Figure 4.1 reported by Liu et *al.*[6]. Furthermore, there is a polarizer angle that yields zero transmission for all quarter-wave plate angles (Figure 4.6 (a)) which demonstrates that the 428 nm emission is linearly polarized. Figure 4.6 (c) further confirms this observation. A summary of the results for different focusing geometry are presented in Figure 4.7.

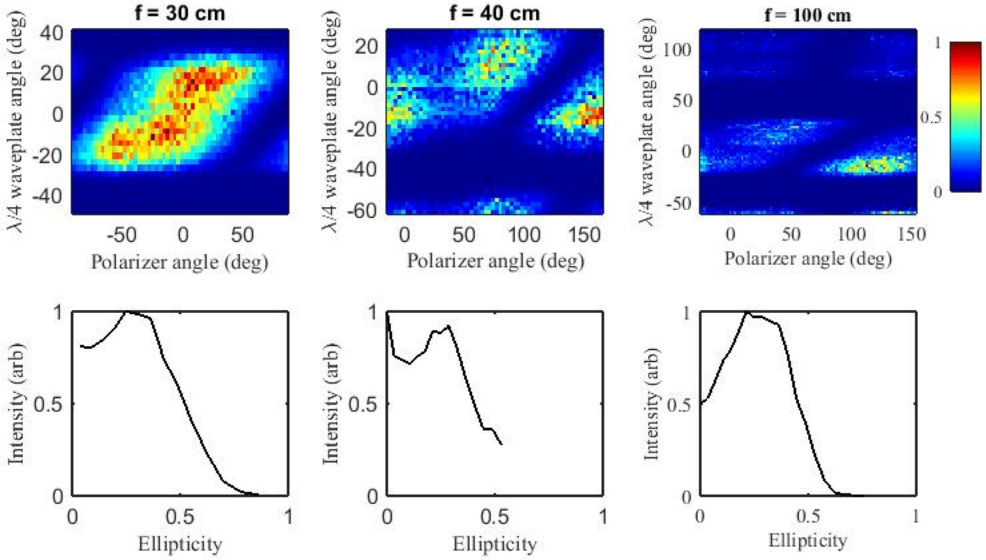

Figure 4.7: Intensity of 428 nm emission (color scale) from air filament as a function of QWP and polarizer angle in degrees for (a) 30 cm, (b) 40 cm, and (c) 100 cm focusing. Normalized intensity of the 428 nm emission as a function of pump pulse ellipticity for (d) 30 cm, (e) 40 cm, and (f) 100 cm focusing.

The raw data for 30 cm, 40 cm, and 100 cm focusing are presented in Figures 4.7 (a), (b), and (c) respectively. The normalized intensity of the 428 nm emission is plotted as a function of ellipticity in Figure 4.7 (d), (e), and (f) for 30 cm, 40 cm, and 100 cm respectively. Each focusing geometry shows slightly different ellipticity dependence. However, a more pronounced increase for nonzero ellipticity is seen for the 100 cm focusing geometry. Note: the polarization rotates more than it did for the unfocused beam due to nonlinear polarization rotation [34].

4.2.3 Experimental Analysis

It is known that continuum generation depends on laser ellipticity [72] which could influence the observed emissions in a filament. Therefore, the ellipticity dependence of the continuum is analyzed near the 428 nm emission (431-455 nm).

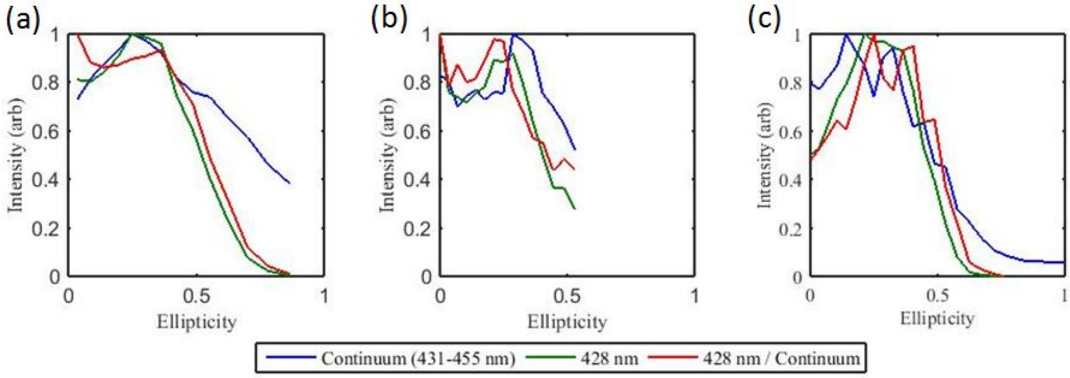

Figure 4.8: Ellipticity dependence of the gain at 428 nm (green), continuum between 431 nm and 455 nm (blue), and 428 nm/continuum (red) for (a) 30 cm, (b) 40 cm, and (c) 100 cm focusing.

The intensity of the selected continuum is shown as a function of ellipticity in Figure 4.8 in blue for (a) 30 cm, (b) 40 cm, and (c) 100 cm focusing. For each focusing geometry, the continuum shows a strong ellipticity dependence. Assuming this part of the continuum acts as the seed to amplify the 428 nm light, its contribution is divided out of the gain and shown in red, giving a value proportional to $e^{gL} - 1$, where g is the gain coefficient and L is the gain length. The resulting gain (shown in red as 428 nm/continuum) for a 30 cm focusing geometry has its maximal value around an ellipticity of 0.45 (Figure 4.8 (a)).

4.3 Summary

In summary, we have studied the lasing emission in N_2^+ in a filament created by an 800 nm femtosecond laser pulse in a self-seeded regime. We focused on the emission at 428 nm from the $B^2\Sigma_u^+(\nu' = 0)$ to $X^2\Sigma_g^+(\nu = 1)$ transition of the first negative band of N_2^+. We experimentally characterized the gain by its ellipticity dependence. The main results are summarized below:

- The emission is linear and follows the major axis of the ellipse.
- The emission shows an enhancement for non-zero ellipticity for all focusing geometry.
- The continuum near the emission has an ellipticity dependence but does not seem to explain the ellipticity dependence of the gain.

Our results suggest that there's a fundamental reason for the enhancement at non-zero ellipticity that is not influenced by filamentation dynamics. To conclude, filaments are relatively complex and chaotic, and therefore, we introduce a more sophisticated method of understanding the gain dynamics in N_2^+ in the following sections of this thesis.

5 The role of recollision in N_2^+ air lasing

5.1 Introduction

In this section, we study the role of electron recollision in N_2^+ lasing by removing the complexity of filamentation. We accomplish this by focusing in a vacuum into a narrow (250 μm) supersonic gas jet. The length of the gain medium is therefore small so that the B-Integral (Equation 3.22) is small. Assuming a gain length of ~500 μm, an intensity of 5×10^{14} W/cm^2, with $n_{2I} = 2.2 \times 10^{-19}$ cm^2/W [73], the B-integral yields a value of ~0.43 for an 800 nm pulse. Therefore, removing the possibility of observing significant nonlinearities that occur in filaments. This setup allows us to make a direct comparison of the ellipticity dependence of the gain and high harmonic generation (HHG). This setup requires us to employ a pump-probe scheme where HHG can be utilized for intensity calibration and to find time-zero between the pulses.

I start by briefly introducing the semi-classical three step model for HHG and the probability of electron recollision. I then move on to talk about the effect of adding ellipticity to the driving pulse and then compare our ellipticity results for the gain in N_2^+ with HHG.

5.2 Introduction to high harmonic generation

5.2.1 The three step model

P.B. Corkum introduced the three step model for HHG in 1993 [74], a semi-classical interpretation of the process. The three step model (illustrated in Figure 5.1) consists of tunnel ionization, acceleration of the tunneled electron, and recombination with the parent ion.

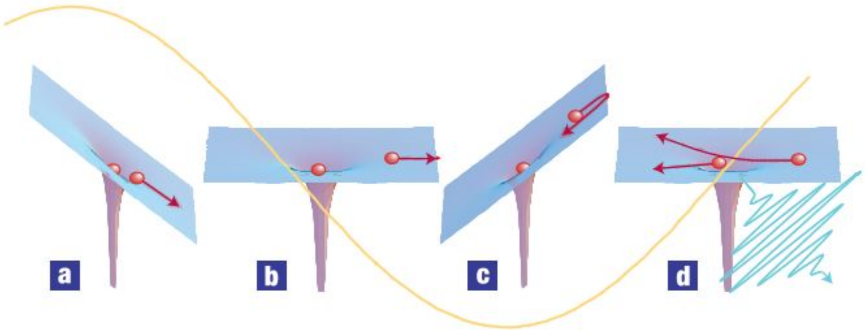

Figure 5.1: The electron is pulled away from the atom (a, b), the electron is driven back after the field reverses (c) where it can recollide with its parent ion (d). Courtesy of Ref. [7]

In the presence of an electric field, the Coulomb potential is suppressed on one side. Under a high enough laser field, a bound electron can tunnel through the modified Coulomb potential into the continuum. The freed electron is then accelerated away from its parent ion by the electric field. The field polarization changes signs every half-cycle, subsequently, the electron is pulled back towards the ion and can then recombine. Consequently, there's a probability a photon with energy equal to the ionization potential I_p plus the gained kinetic energy acquired by the laser field E_k can be emitted.

$$\hbar\omega = I_p + E_k \tag{5.1}$$

The maximum energy acquired by the electron is $E_k = 3.17U_p$ [75], where U_p is the ponderomotive energy given by

$$U_p = \frac{e^2 E_0^2}{4m_e\omega_0^2} \tag{5.2}$$

where e is the electron charge, E_0 is the field amplitude, m_e is the electron mass, and ω_0 is the fundamental frequency of the driving laser field. Due to inversion symmetry, the emitted harmonics are only odd multiples of the fundamental frequency.

5.2.2 Ellipticity dependence of HHG

The motion of a free electron usually takes place in the direction of the driving laser polarization. Therefore, HHG is highly dependent on the ellipticity of the driving laser field. The electron that is freed by tunneling is deflected by following the trajectory of an elliptically polarized laser field. Consequently, the probability of recombining with its parent ion is reduced significantly[76, 77].

5.2.3 Population transfer by recollision

The radiative recombination in the HHG process is not an absolute requirement. In fact, electron recollision may excite other electrons instead of releasing photons. The recombining electron can collide with an inner orbital electron, and if it has enough energy, it can excite the inner orbital electron to the outer orbital of the ion. This process in the case of N_2^+ air lasing can only occur if the returning electron gained at least 3.17 eV of kinetic energy (the energy difference between the two states involved). The calculations performed by my colleague show that some population transfer between these states is possible by recollision[78]. However, the total population transfer is calculated to be less than 4% for intensities less than $1 \times 10^{15}\ W/cm^2$. Therefore, it seems unlikely that a population inversion can be achieved this way but recollision can still play a role.

5.3 The experiment

5.3.1 Experimental setup

The pump-probe experimental setup is illustrated in Figure 5.2. A commercial Ti:sapphire laser system (Legend Elite Duo, Coherent, Inc.), operated at a repetition rate of 1 kHz and provided ~42 fs (full-width half-maximum (FWHM) intensity profile) Fourier-transform-limited pulses with a center wavelength of 800 nm and a pulse energy of ~5 mJ. The laser beam is first split into two arms using a 70:30 beamsplitter (70% reflective and 30% transmissive). The reflected laser beam is passed through a half-wave plate (HWP) and then onto a reflective polarizer for intensity control and then onto a delay stage. A HWP followed by a quarter-wave plate (QWP) is then used for ellipticity control. The transmitted laser beam was frequency doubled using a 0.2 mm-thickness Beta Barium Borate (BBO) crystal to act as a probe to seed emission at 391 nm and 428 nm in N_2^+. The fundamental frequencies are filtered by a blue band-pass filter and the frequency doubled beam is passed through a HWP and polarizer for intensity control. The two laser beams are recombined at a dichroic mirror with high reflectivity at 400 nm and high transmission at 800 nm. The beams are then focused in a vacuum chamber using an 30 cm focusing mirror where a thin gas jet is located near the focus. The beams are then imaged onto a fiber-spectrometer by a 30 cm fused silica lens. The gas jet has an opening of ~250 microns and a backing pressure of ~6 bar and is operated at 500 Hz.

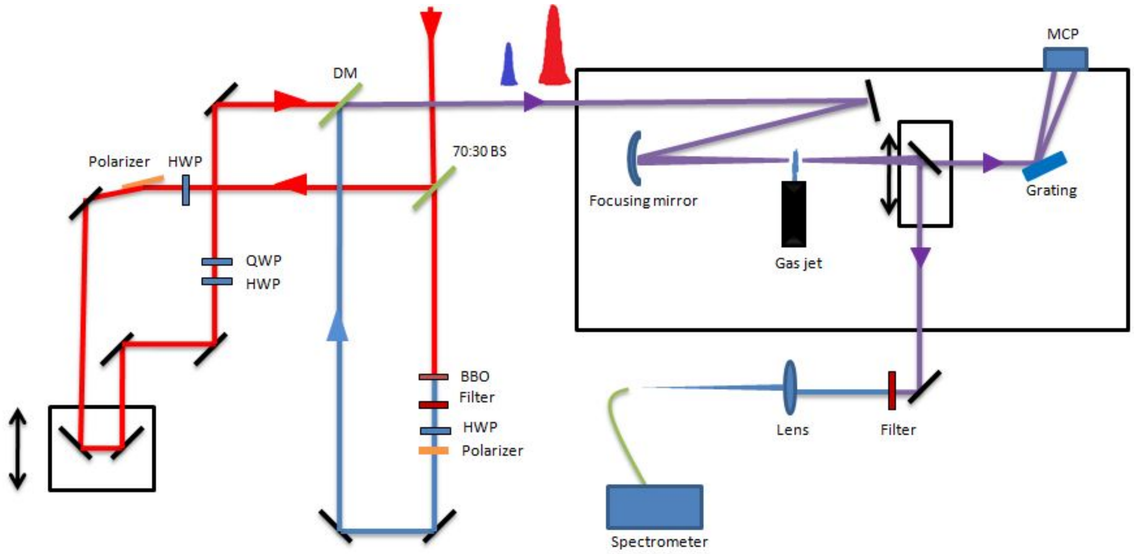

Figure 5.2: Pump-probe experimental setup.

The beam waist is calculated to be 21 microns for 800 nm and 11 microns for the 400 nm beam and therefore it is reasonable to assume that we probe within the gain region. The Rayleigh range is calculated to be $Z_R = \pi\omega_0^2/\lambda =$ 1.73 mm which is longer than the gain medium and therefore we may assume that we have a uniform intensity profile throughout the gain medium and the gain region should stay of constant length for a fixed gas jet position throughout the experiments.

Figure 5.3 (a) shows the transmitted pump pulse while traveling only through the vacuum and while traveling through the nitrogen gas. A small absorption/deflection is observed, however, we observe no significant spatial or spectral distortion of the pump pulse, so we must use the probe pulse to seed the gain. Figure 5.3 (b) shows a typical spectrum of the measured probe pulse with the pump at a reasonable delay (~0.4ps) arriving before the probe. The probe shows clear amplification at 391 nm while the pump pulse is active. The 428 nm signal can also be observed by tuning the BBO angles to get photon counts at 428 nm.

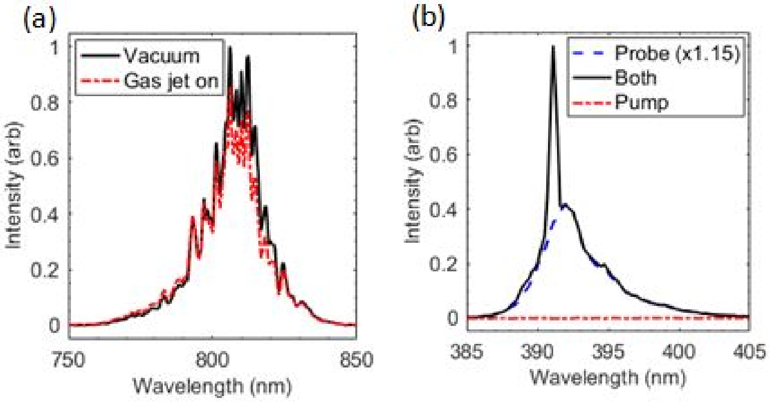

Figure 5.3: (a) Pump pulse modification while traveling through the gas jet. (b) Probe pulse modification due to the pump pulse.

It should be noted here that only one peak is present corresponding to the P branch transition while the R branch is not resolved due to the limited resolution of our spectrometer. The R branch emission is also known to be much weaker and could be present within the noise.

A movable mirror is used to allow the laser beam to travel to a grating-Multichannel plate (MCP) where we can detect harmonics. Even harmonics are used to accurately find zero delay between the pump and probe pulses. The cutoff of the odd harmonics are used to find our real intensity at the focus through the well known cutoff law [75] [See Appendix A].

5.3.2 Pump ellipticity dependence of the gain in N_2^+

We start by creating a coherent rotational wavepacket by focusing the pump pulses in the nitrogen gas target. Then by delaying the pump relative to the probe we observed the real time dynamics of the gain in N_2^+. Figure 5.4 (b) shows such wavepacket and is studied in more details in Section 6.

Here we study the gain yield in N_2^+ as a function of the ellipticity of the pump laser pulses. The ellipticity of the pump is varied from linear (parallel to the probe) to circular and then from circular to linear (perpendicular to the probe). The ellipticity dependence of the gain (gL) at 391 nm is shown in Figure 5.4 (a) for different pump-probe time delays as shown with vertical lines in Figure 5.4 (b) where gL is defined as the gain coefficient g in cm^{-1} multiplied by the gain length L where $gL = \log(I_{out}/I_{in})$.

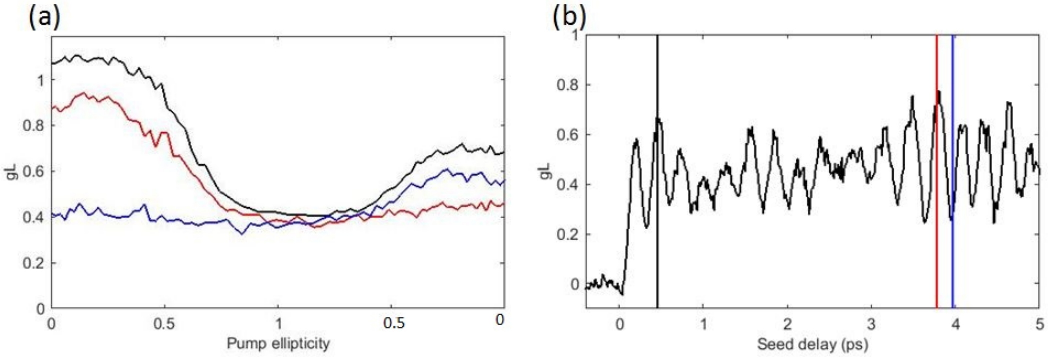

Figure 5.4: (a) Ellipticity dependence of the gain at 391 nm for three different probe delays. (b) Time evolution of the gain with selected regions of interest. The first two vertical lines (black and red) are at times of alignment while the blue line is at a time of anti-alignment.

The results show an increase for non-zero ellipticity, similar to our observations in a filament. However, we measure significant gain for circular pump ellipticity which, to our knowledge, we are the first to report.

The emission is dependent on the polarization difference between the pump and probe. The results show a higher gain when the pump and probe have the same polarization which is consistent with previous observations [79, 12]. However, our results show that this is dependent on the alignment of the molecules. Figure 5.4 (a) shows that during time of anti-alignment of the rotational wavepacket (blue line in Figure 5.4 (b)), the gain prefers a pump that is perpendicular to the probe.

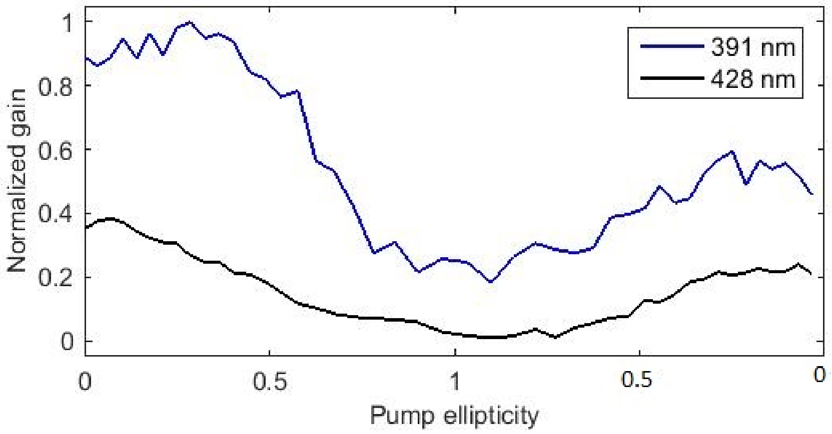

Figure 5.5: Ellipticity dependence of the gain at 391 nm and 428 nm.

The 391 nm and 428 nm emission lines show similar behaviors as shown in Figure 5.5. The main difference is where the maximum gain is located. At the wavelength of 391 nm we observe a maximum gain at an ellipticity of ~0.3 while the 428 nm is closer to ~0.1.

As presented in Section 4, it was suggested that electron recollision plays a significant role in establishing a population inversion between the $B^2\Sigma_u^+$ and $X^2\Sigma_g^+$ states in N_2^+. Our findings suggest otherwise for two reasons;

- Simple molecules such as N_2 does not show an increase in HHG yield as a function of ellipticity,
- There is also usually no observable HHG yield for circular pumping.

Our experimental setup allows us to compare the HHG yield with what is observed in the 391 nm and 428 nm emissions. The harmonics are observed by a grating MCP configuration. Figure 5.6 shows a comparison of the ellipticity dependence of HHG with N_2^+ lasing.

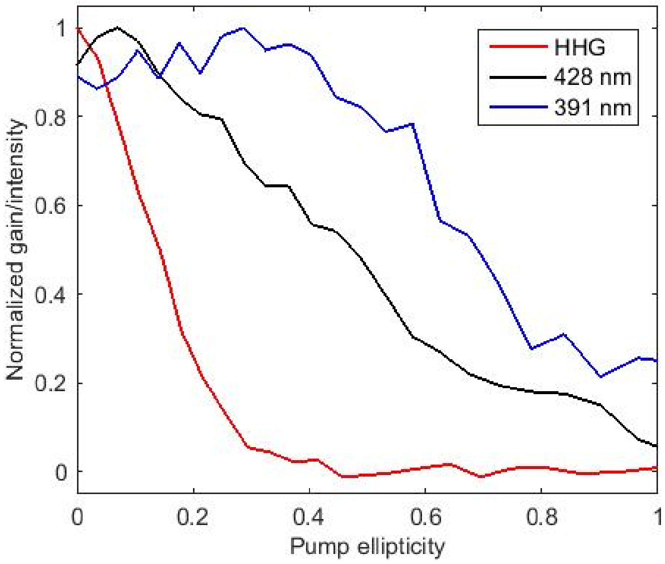

Figure 5.6: Ellipticity dependence of the gain at 391 nm and 428 nm for a pump intensity of $4 \times 10^{14}\ W/cm^2$, and the harmonic yield, also as a function of ellipticity.

Our HHG results show a strong ellipticity dependence with no increased yield with ellipticity. It's important to remember that the N_2^+ emissions are intensity dependent. Therefore, we retook the 391 nm measurements at reduced intensities to compare with intensities seen in filaments. Results for two different intensities are plotted in Figure 5.7.

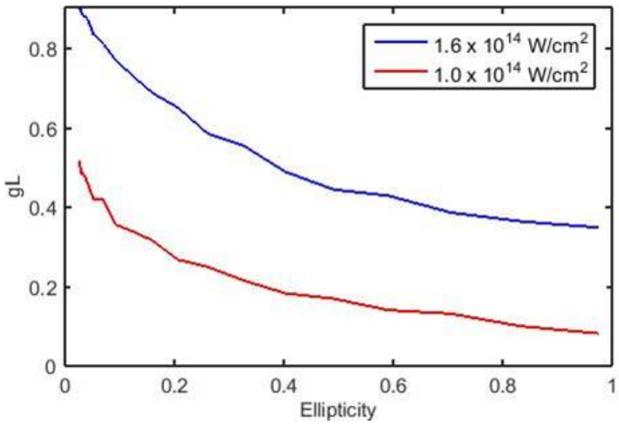

Figure 5.7: Ellipticity dependence of the gain at 391 nm for two intensities that are similar to intensities seen in filaments.

To our surprise, the ellipticity behavior of the gain is quite different in this intensity regime when comparing to the results presented in the previous figures. More experimental and theoretical investigations of the ellipticity dependence of the measured gain are required to understand this effect. However, one thing is consistent, and that is that gain is observed for a circularly polarized pump.

5.4 Summary

In summary, we have studied the lasing emission in N_2^+ at 391 nm and 428 nm wavelengths as a function of ellipticity using a pump-probe scheme. The ellipticity dependence of the gain at different times of alignment of the rotational wavepacket (aligned and anti-aligned) show different behavior. We also compared the ellipticity dependence of the gain with the generated harmonics. The main results are summarized below:

- A pump parallel to the probe will yield higher gain than a pump perpendicular to the probe.
- The gain shows an enhancement for non-zero ellipticity for higher intensities, however, at lower intensities, this enhancement disappears.
- The gain does not show similar behavior as HHG as a function of ellipticity, and there is gain at circular polarization for all our measurements.

It seems reasonable to conclude that recollision doesn't play a significant role in creating an inversion between the $B^2\Sigma_u^+$ and $X^2\Sigma_g^+$ states in N_2^+. Therefore, we search for new potential mechanisms in the following sections.

6 N_2^+ lasing in a thin gas jet

6.1 Introduction

The experimental setup introduced in Section 5 has many advantages to study the gain dynamics of a system such as N_2^+. In this section, we study the time dependence of the gain, the intensity dependence, the gas jet position, and the plasma density. The following experiments are performed using linear polarization where the pump and probe pulses are parallel to each other.

6.2 Time evolution

The pump-probe scheme allows us to observe the ultrafast dynamics of the gain. The results of such pump-probe measurements are shown in Figure 6.1 for the lasing emissions at 391 nm and 428 nm. We measure a fast gain buildup followed by a slower decay in agreement with previous observations [64, 79, 12, 80, 81]. Very strong periodic modulations appear on the measured gain curve around 2 ps, 4 ps, 6 ps and so on. These modulations can be assigned to $T_{rev}/4$, $T_{rev}/2$ and $3T_{rev}/4$ revival times of the rotational wavepacket of the $B^2\Sigma_u^+$ state of N_2^+ having a rotational period of $T_{rev} = 8.03$ ps. This is calculated using equation 2.11 with a rotational constant of $B = 2.07456$ cm^{-1} [82].

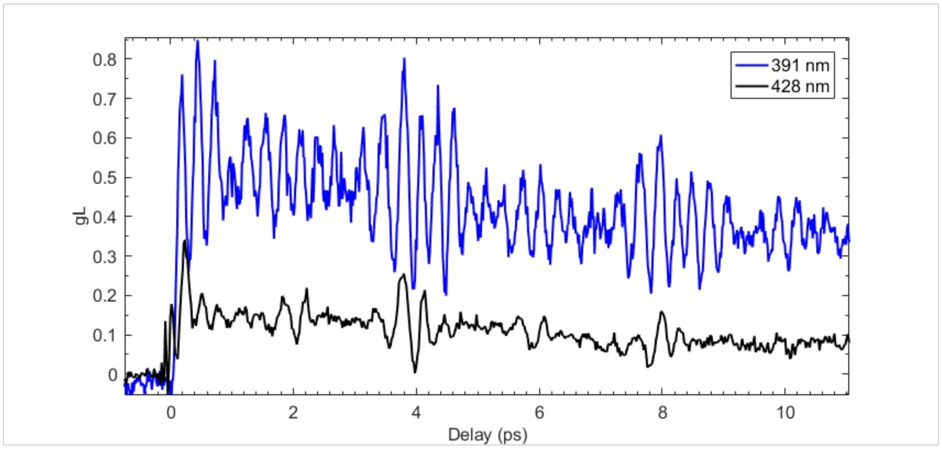

Figure 6.1: Gain as a function of pump-probe delay for the 391 nm and 428 nm emission lines for a pump beam with intensity of $6 \times 10^{14}\ W/cm^2$.

The rotational constant for the $X^2\Sigma_g^+$ state is $B = 1.93176\ cm^{-1}$ [82] which represents a rotational period of $T_{rev} = 8.63$ ps. It, therefore, seems unlikely that the $X^2\Sigma_g^+$ state wavepacket is dominant in these results, but, some overlap might be possible due to the length of the measured revivals of the wavepacket extending over 1 ps. The intensity of the generated gain at 428 nm is lower than that of the 391 nm gain for this pump intensity. The intensity dependence of the gain will be further explored in section 6.3.

Figure 6.2 shows a zoomed-in view of the half revival of the 391 nm and 428 nm gain where the decay is divided out for comparison purposes. We notice that both emission lines have a slightly different rotational wavepacket.

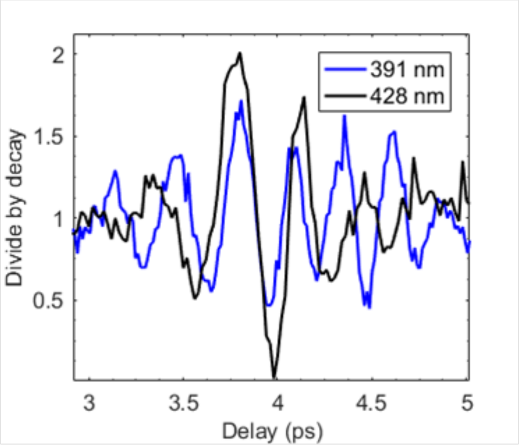

Figure 6.2: Comparison of the half revival of the rotational wavepacket of the 391 nm and 428 nm gain.

The revival structure of the rotational wavepacket of the 428 nm is slightly stretched (i.e., lasts longer) compared to the 391 nm. This observation is consistent for all fractional revivals including the full revival. A final observation that we make is the difference in the decay time of the gain curve of the 391 nm and 428 nm. The 428 nm gain curve always shows a quicker decay time than the gain at 391 nm. These emission lines are associated with the same excited $B^2\Sigma_u^+(\nu = 0)$ state but different vibrational states ($\nu = 0$ for 391 nm and $\nu = 1$ for 428 nm) in the ground $X^2\Sigma_g^+$ state. The $\nu = 0$ state is primarily populated by ionization.

Other works have analyzed these time domain results in the frequency domain by performing a Fourier transform on similar curves [79, 83, 12]. These provide very high-frequency resolution and provide information on the rotational levels involved. It was demonstrated that the rotational states involved come from both the $B^2\Sigma_u^+$ and $X^2\Sigma_g^+$ states [12, 83].

6.3 Intensity dependence

An easy measurement to do with this experimental setup is to vary the pump laser intensity, which we have complete energy control with a half-wave plate and polarizer in the pump arm. These measurements are hard to do in the filament regime where the intensity is clamped. Figure 6.3 shows the time dependence of the gain for three different intensities from the 391 nm emission line. These measurements are done in a region where the focus is very near to the gas jet opening.

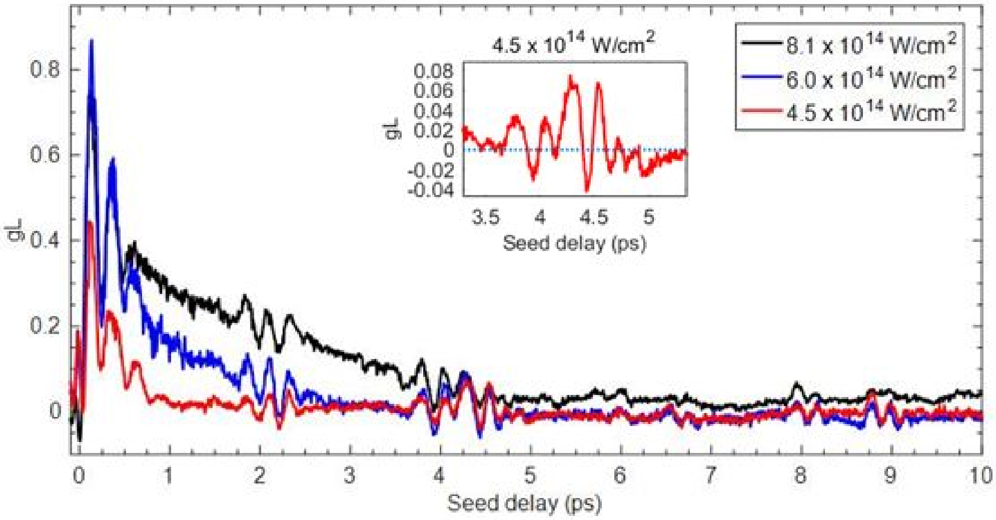

Figure 6.3: Gain as a function of pump-probe time delay for three different intensities. Inset: Half-revival for an intensity of $4.5 \times 10^{14}\ W/cm^2$.

Some key characteristics of the gain dynamics are shown in this figure. We observe an intensity dependence of the decay of the gain as a function of time. As the intensity is reduced, the gain is very short lived. Surprisingly, we observe revival structures of the rotational wavepacket at times where the gain has decayed completely. The gain dynamics at these revivals seem to periodically show absorption followed by emission (see Figure 6.3 inset).

Note: Figure 6.3 shows revival structures at odd revival locations around 9 ps. Oxygen has a rotational period T_{rev} of 11.601 ps [84] which means a $3T_{rev}/4$ of 8.7 ps while nitrogen has a rotational period T_{rev} of 8.383 ps [85]. It seems that a rotational wavepacket is created in the air along the way with an additional delay from the glass window going to the vacuum chamber can explain these[1].

On the other hand, the peak intensity of the gain at 391 nm has a downward trend for reduced intensity. Figure 6.4 shows the measured gain as a function of intensity for the transitions at 391 nm and 428 nm.

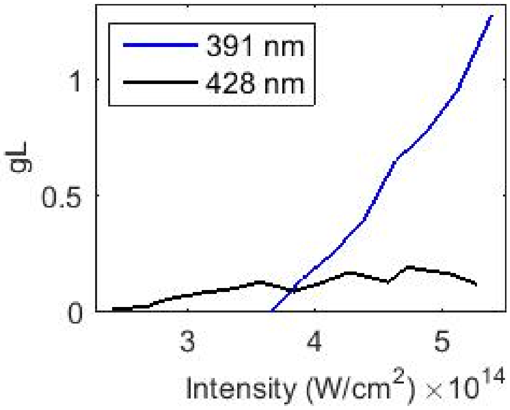

Figure 6.4: Pump intensity dependence of the gain for 391 nm and 428 nm emission lines.

Both emission lines show different behaviors. The 391 nm emission line shows a steep near linear increase of the gain as a function of intensity. However, the gain at 428 nm only shows a small dependence with intensity. At smaller intensities (below $\sim 3.6 \times 10^{14}$ W/cm^2) the 428 nm emission seems to become the dominant emission line[2].

---

[1] In fact, my colleagues have confirmed this by fitting the oxygen and nitrogen wavepackets to the data.

[2] Only the general trend should be acknowledged but not the actual values. As we have seen in Section 5, we where able to reduce the intensity of the 391 nm significantly.

6.4 gas jet positions

The gas jet used in the experiment can be moved remotely in all three dimensions. We use this convenience to optimize our lasing signals. However, by varying the gas jet position transversly to the laser beam, we change the gain length and density. Figure 6.5 shows how the gain dynamics of the 391 nm transition varies with the gas jet position for four different positions (0 μm, 250 μm, 500 μm, and 750 μm). The 0 μm position is defined as the closest position the gas jet can be from the gain medium without causing damage while 750 μm is the furthest possible where we still observe some gain.

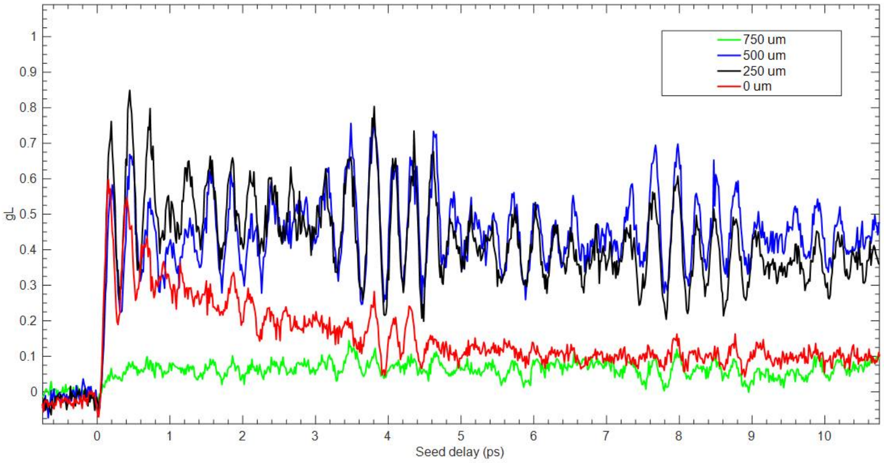

Figure 6.5: Gain as a function of probe delay for four different jet positions. The 0 μm position is defined as the closest position to the jet while 750 μm is the furthest position.

At the closest position, we measure a few picoseconds decay of the gain. However, as the gas jet is backed away from the gain medium, the decay time becomes significantly longer. This behavior of the gain seems to indicate that free electron collisions in the plasma are killing the gain. This is because, at lower densities, free electrons have a smaller frequency for collisions. However, in this setup, we change both the gain g and the length L in the amplification ratio e^{gL} and thus, we can't make firm conclusions on the decay mechanism yet. We explore this effect further in the next section using mixed gases.

Another interesting effect we measure is the enhancement of the rotational wavepacket at further distances of the gas jet opening. We attribute this to the cooler distribution of rotational states as the gas expands in the vacuum chamber.

6.5 N_2/He gas mixtures

To investigate the decay of the gain with the gas jet position we can keep the length of the gain medium constant and change only the gain g. We do this by using different mixtures of molecular nitrogen and helium. The ionization energy of helium is 24.6 eV, which is much larger than 15.58 eV for molecular nitrogen. Therefore, we assume that we would not ionize helium in our experimental conditions. This allows us to change the number of free electrons in the plasma. The time evolution of the gain at 391 nm is presented in Figure 6.6 for 100% N_2(black curve), 50% N_2 and 50% He (red curve) and, 25% N_2 and 75% He (blue curve).

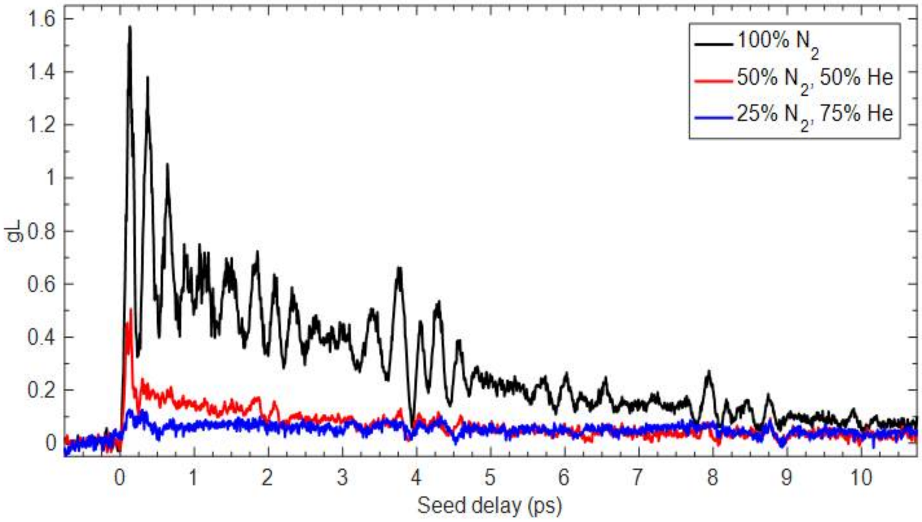

Figure 6.6: Time evolution of the gain at 391 nm for 100% N_2 (black curve), 50% N_2 and 50% He (red curve) and, 25% N_2 and 75% He (blue curve).

We measure a decrease in the intensity of the signal as a function of increased helium concentration due to the reduced number of N_2^+. The value of gL at a delay of 0.13 ps is plotted in Figure 6.7 (a) as a function of the square of the concentration showing a linear trend. This quadratic behavior with the number of emitters is a signature of the superradiant behavior of N_2^+ (discussed in section 7.5). Furthermore, we measure a slower decay time of the gain for increased concentration of helium in the mixture. This implies a direct relationship between the decay of the gain and the density. I extracted the decay time for each gain curves and the inverse exponential decay constants are plotted as a function of concentration in Figure 6.7 (b).

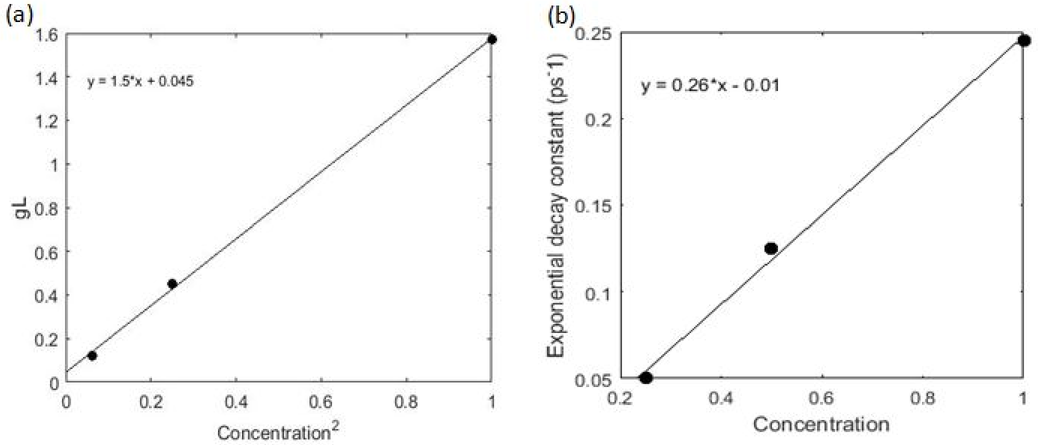

Figure 6.7: (a) Gain as a function of the concentration square of N_2. (b) Inverse exponential decay constants as a function of the concentration of N_2.

As expected from electron collisions, the decay of the gain is inversely proportional to the concentration (i.e., the density). This is an indication that the fast decay of the gain is due to free electron collisions.

6.6 A second gain mechanism

As seen in all the previous results in this section, gain at 391 nm and 428 nm shows a clear rotational wavepacket. In this section, we present findings that suggest an alignment condition where we see the enhancement of the seed pulse but lose the rotational wavepacket. So far all experimental results presented are done by collinearly propagating pump and probe pulses. We found that amplification is still observed if we misalign the pump pulse with respect to the probe. In fact, we can measure larger amplification in this setup.

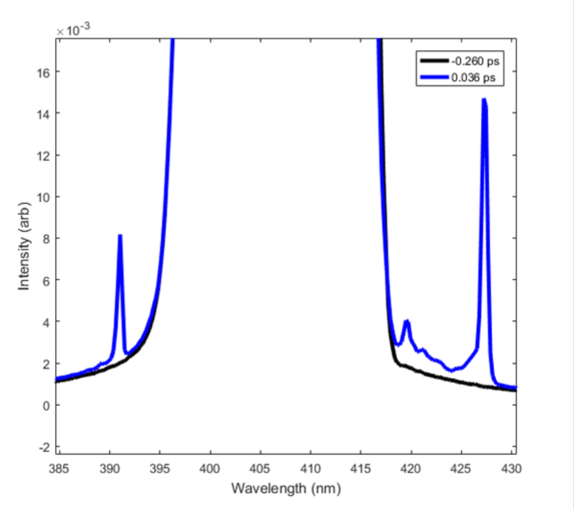

Figure 6.8: Spectrum of the observed gain at 391 nm, 420 nm, and 428 nm for a slightly misaligned pump and probe beams.

To our surprise, not only did we see amplification at 391 nm and 428 nm but also at 420 nm as shown in Figure 6.8. The 420 nm emission line is attributed to the transition between the vibrational states $\nu' = 2$ and $\nu = 3$ between the $B^2\Sigma_u^+$ and $X^2\Sigma_g^+$ states respectively. Figure 6.9 shows the time evolution of this amplification effect.

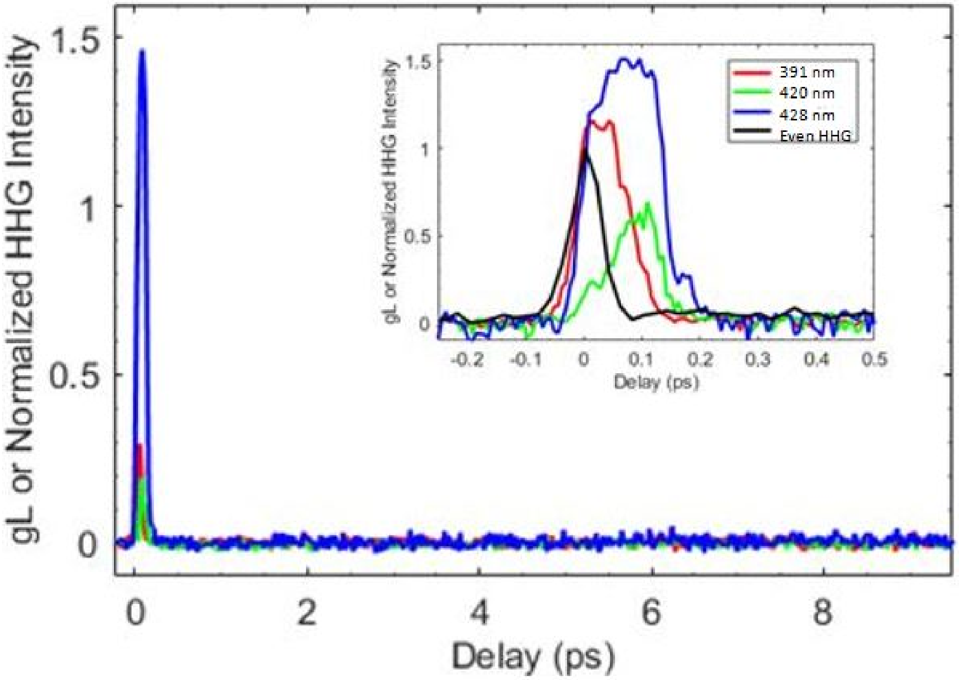

Figure 6.9: Time dependence of the emission at 391 nm, 420 nm, and 428 nm. Inset: Comparison near zero delay with even harmonics.

To our knowledge the emission line at 420 nm has only been reported by J. Ni et *al.* where they report simultaneous emissions at 420 nm, 424 nm ($\nu' = 1 \rightarrow \nu = 2$) and 428 nm[86]. However, it seems that no experimental or theoretical investigation has been conducted.

The emission process in this configuration is present only around zero delay. The inset in Figure 6.9 shows a comparison of the time evolution of this amplification with reference to the observed even harmonics. Clearly, no wavepacket is observed, and the buildup of the emission and decay show slightly different behaviors for different emission lines. Explaining this emission process is of interest to the air lasing community since in filaments it would be indistinguishable from our "traditional" gain. We currently attribute this amplification to some nonlinear effect such as wave-mixing.

6.7 Summary

In summary, we have studied the lasing emission in N_2^+ created by an 800 nm femtosecond laser pulse in a pump-probe scheme. The 391 nm and 428 nm emissions belong to the $B^2\Sigma_u^+(\nu' = 0)$ to $X^2\Sigma_g^+(\nu = 0, 1)$ transitions of the first negative band of N_2^+. We experimentally characterized the gain by its temporal profile, pump intensity dependence, gas density dependence, and pump alignment dependence. The main observations are summarized below:

- The gain shows an ultrafast gain build-up of ~ 200 fs, which is independent of the pump intensity, gas density, and pump pulse ellipticity
- The gain decays in a time scale of a few picoseconds and the decay becomes quicker for lower pump intensity, and higher gas density
- The gain is modulated by molecular revivals of the rotational wavepacket which shows revival structures at $T_{rev}/4$, $T_{rev}/2$, $3T_{rev}/4$ and so on, and they seem to persist after the decay of the gain.
- The 391 nm emission behaves differently than the 428 nm in the sense that the decay of the 391 nm is quicker, the wavepacket is slightly different, and they have a different intensity dependence.
- Amplification at 391 nm, 420 nm, and 428 nm was observed under different pump alignments. This amplification effect is only observed around zero delay and shows no revival structures of a rotational wavepacket.
- The gain shows signs of superradiance as the intensity varies as N^2 and the decay as $1/N$ where N is the number of emitters and is proportional to the density of the gain medium.

7 Discussion

7.1 Properties of N2+ lasing

7.1.1 Ultrafast gain buildup

In this thesis, many measurements of the gain in N_2^+ at 391 nm and 428 nm as a function of time were done. Throughout all the measurements we always measured an ultrafast gain buildup of about ~200 fs and this did not change drastically with different experimental conditions. The lasing in the neutral nitrogen, which emits at 337 nm, has a pressure dependent gain buildup that is well understood now through collisional excitation[87]. However, as seen from our concentration scan from Figure 6.6, the 391 nm gain buildup of N_2^+ does not depend on plasma density. This leads us to reject the possibility of electron excitation as a possible excitation mechanism in N_2^+.

The ultrafast gain buildup also suggests that gain seems to be established during the duration of the pump laser pulse. Therefore, strongfield ionization is probably responsible for establishing gain in this system.

7.1.2 Fast decay

The duration of the gain in N_2^+ is on the order of several picoseconds to hundreds of picoseconds depending on gas density and laser intensity. Our experimental measurements of the plasma density (see Figure 6.6) and pump laser intensity (see Figure 6.3) suggest that free electron collisions are responsible for the fast decay of the gain in N_2^+. Increasing the pump laser intensity gives extra energy to free electrons, and therefore, reduces the frequency of collisions. A reduction in collisions is also true for decreasing gas densities. However, a recent group (M.Lei et *al.*) studied the evolution of the population of the $B^2\Sigma_u^+$ state as a function of free electron density to conclude that the decay might be due to collisions between the free electrons and the $B^2\Sigma_u^+$ state[88]. Experimental evidence seem to indicate that electron-ion collisions could be responsible for the fast decay of the gain. However, the decay could also come from the thermalization of free electrons. In order to confirm the mechanism behind the decay of the gain, the temperature needs to be well approximated as well as the density.

7.1.3 Superradiance behavior

It was suggested that lasing in N_2^+ shows signatures of superradiance [9]. In this section, I will introduce the concept of superradiance and the experimental evidence for such claim.

Superradiance was first described mathematically by R. Dicke in 1954 regarding spontaneous emission[89]. If a low concentration atomic system is prepared in an excited state, it will eventually decay by spontaneous emission (i.e., by the interaction with the vacuum fluctuations) and the atoms can be considered to be independent. This emission process obeys an exponential decay law that takes a characteristic time τ_{sp} as shown in figure 7.1 (a) and this emission is isotropic.

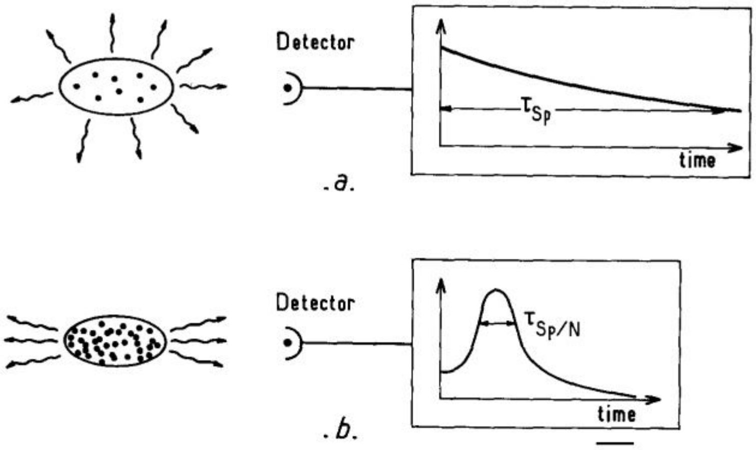

Figure 7.1: Comparison between the general characteristics of spontaneous emission and superradiance. (a) Ordinary spontaneous emission is essentially isotropic with an exponentially decaying intensity (time constant τ_{sp}). (b) Superradiance is anisotropic with an emission occurring in a short burst of duration τ_{sp}/N where N is the atom number. Courtesy of Ref. [8].

If the number of emitters N becomes sufficiently large, the above process can be altered. It this case, the ensemble of emitters will emit spontaneously much faster and stronger than the emission of independent atoms or molecules (see figure 7.1 (b)). Depending on the geometry of the ensemble, the spontaneous emission radiates in a well-defined direction[8]. Dicke called this process "superradiance".

A way to understand this process is that the emitters are close enough together that spontaneous emission of a photon from one emitter is seen by its neighbors. This photon is seen as phase coherent and will stimulate emission. Unlike incoherent emission having an emission intensity dependence that is proportional to the number of emitters N, the emission of this "cooperative" process is proportional to N^2. The emission is no longer exponential but occurs in a short bursts of duration τ_{sp}/N as seen in figure 7.1 (b) and decay time proportional to $1/N$. These are the main features of superradiance.

G. Li et *al.* was the first to demonstrate that N_2^+ lasing between the $B^2\Sigma_u^+(\nu = 0)$ and $X^2\Sigma_g^+(\nu = 0)$ state showed superradiance behavior[9]. They studied the temporal profile of the 391 nm emission as a function of filament length (i.e., number of emitters). Their findings included a delay between the seed pulse and the lasing emission as well as a decreasing characteristic time of emission (τ_{sp}/N) with increasing filament length, both of which agree well with the behavior of superradiance. The superradiant behavior of the gain has then been further confirmed experimentally [6].

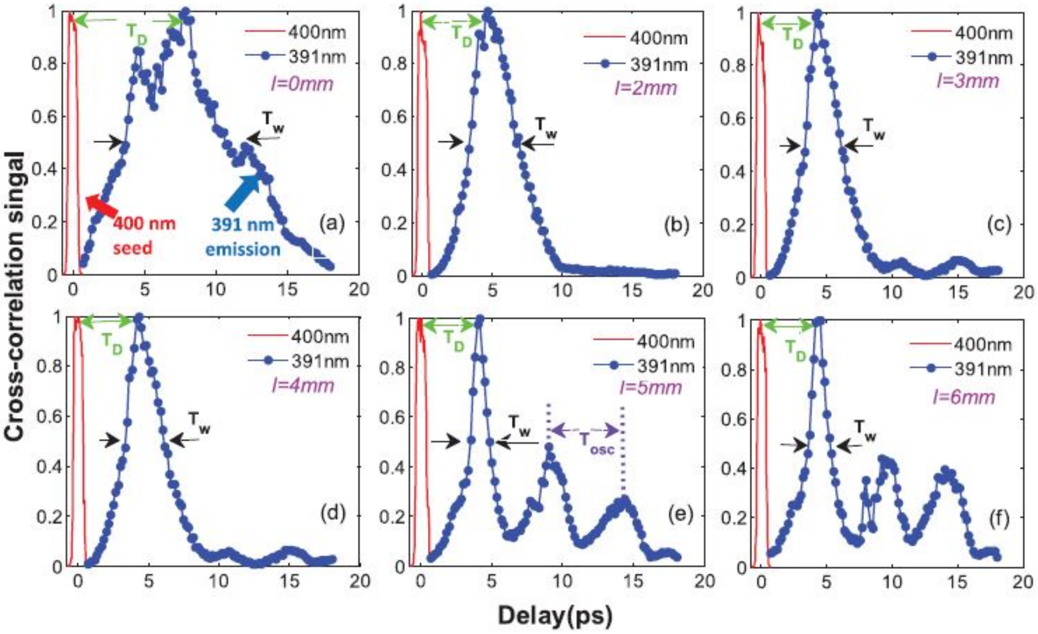

Figure 7.2: (a) Time-resolved cross-correlation signals of the 800-nm with the 400-nm seed pulses (solid red line) and the 391-nm coherent emissions (blue line with circles) for the plasma channel lengths of (a) 0 mm, (b) 2mm, (c) 3 mm, (d) 4 mm, (e) 5 mm, (f) 6 mm, respectively. Courtesy of Ref. [9].

Our results presented in Figure 6.7 also show the expected N^2 behavior of superradiance.

7.2 Possible gain mechanisms

The gain mechanism responsible for the N_2^+ lasing action is still not well understood. Since population inversion is not a prerequisite to obtain optical "gain", it is still unclear if population inversion is achieved in this system. The next subsections discusses several proposed gain mechanisms that require population inversion and several that don't.

7.2.1 Electron recollision

Electron recollision excitation has received a lot of attention lately due to the highly similar dependence of the gain with pump pulse ellipticity compared to the ellipticity dependence of the yield for high harmonic generation and was first proposed by Y. Liu et *al.* [6] (see Figure 4.1). The process of HHG can be well explained by the semi-classical recollision model[74] which was briefly introduced in Section 5. It's well known that simple molecules don't exhibit a nonzero enhancement with ellipticity as seen in the N_2^+ gain. It's also known that there is no HHG yield for a circularly polarized pump since the freed electron is prevented from recolliding with its parent ion.

Our experimental measurements shows that the nonzero enhancement with ellipticity is not a consequence of filamentation and must be explained by the gain mechanisms in question. Furthermore, we measure significant gain for a circular pump (see Figure 5.6) in a thin gas jet. Therefore, we conclude that if this gain mechanism plays a role, it is small.

7.2.2 Natural population inversion

It has been suggested that any small molecule possessing excited ionic states which are energetically close to the ionic ground state could be pumped inside a femtosecond laser filament into a population-inverted system as long as the molecule is not yet fragmented [90]. N_2^+ being one such molecule it was proposed that three-photon absorption from the ground X state to the excited B state, or a four-photon process involving higher vibrational levels of the excited state could give rise to gain. This would be a mechanism of population inversion that is universal. There is, however, no experimental confirmation for this theory.

7.2.3 Multiple state coupling

Two different groups have made theoretical simulation based on the time-dependent Schrodinger equation to show that population inversion between the $B^2\Sigma_u^+$ state and the $X^2\Sigma_g^+$ state of N_2^+ can be established by population exchange between different states[10, 91]. They show that immediately after ionization of N_2, the population mostly end up in the ground state of N_2^+. After which, the laser field causes most of the population from the $X^2\Sigma_g^+$ state to be redistributed between the $A^2\Pi_u$ state and $B^2\Sigma_u^+$ state by Rabi oscillations.

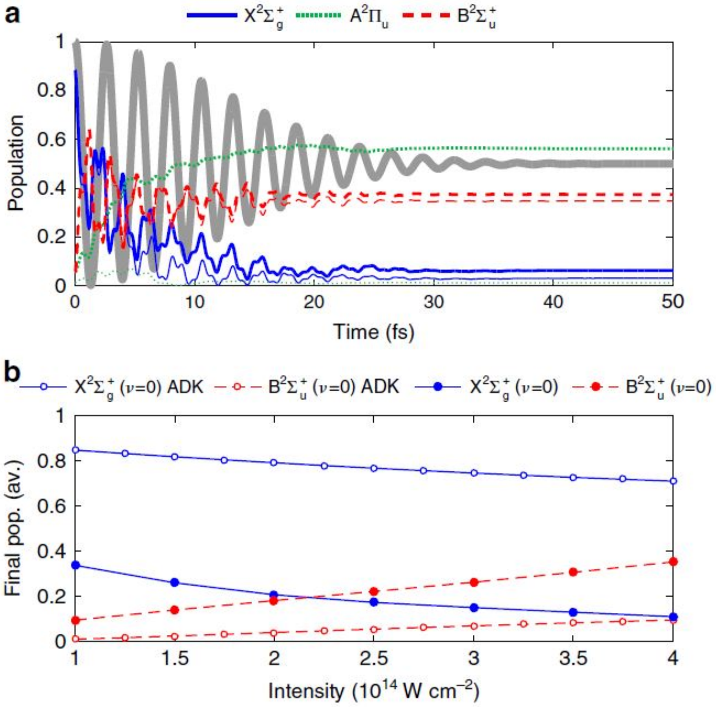

Figure 7.3: Population inversion of N_2^+ in a 20-fs laser pulse. (a) Time dependent populations of the three electronic states in a laser pulse with a FWHM of 20 fs, assuming ionization at $t = 0$. Thick lines represent the total population in all vibrational states, and thin lines correspond to the populations in the vibrational ground states. The laser field (not to scale) is plotted in the background. (b) Final populations in the vibrational ground state of the $X^2\Sigma_g^+$ state (solid lines), and of the $B^2\Sigma_g^+$ state (broken lines). The case when only tunnelling ionization is included (open symbols) and when tunnelling ionization and post-ionization dynamics is included (solid symbols). Courtesy of Ref. [10].

Figure 7.3 shows a simulation from H. Xu et *al.* [10] for a 20 fs FWHM laser pulse. As seen in Figure 7.3 (a), after ionization, the population is mostly redistributed in the $A^2\Pi_u$ state and a population inversion between the $B^2\Sigma_u^+$ state and $X^2\Sigma_g^+$ state is established. In other words the $A^2\Pi_u$ state can act as a population trap to achieve inversion. Figure 7.3 (b) shows that the population inversion is intensity dependent and that inversion can be established for a 20 fs pulse for intensities above 2.2×10^{14} W/cm^2. It's interesting to note that population inversion is achieved between the $A^2\Pi_u$ state and the $X^2\Sigma_u^+$ state and, if this model is correct, lasing could be observed for this transition.

7.2.4 Inversion free transient gain

A. Baltuska et *al.* proposed that gain can be achieved between the $B^2\Sigma_u^+$ state and $X^2\Sigma_g^+$ state without population inversion[11]. They suggest that during times of rotational alignment of the molecules, there could be more aligned molecules in the excited state relative to the ground state. Since the probability of transition (W) is proportional to the product of the population (P) of the final state and the alignment factor ($< cos^2(\theta) >$) of that state, $W_{down} > W_{up}$ can be achieved. The probability of absorption from $X^2\Sigma_g^+$ state to $B^2\Sigma_u^+$ state is

$$W_{up} \propto < cos^2(\theta)_X > P_X \tag{7.1}$$

and the probability of stimulated emission from $B^2\Sigma_u^+$ state to $X^2\Sigma_g^+$ state is

$$W_{down} \propto < cos^2(\theta)_B > P_B \tag{7.2}$$

where W_{up} is the probability of an upwards transition (absorption) and W_{down} is the probability of a downward transition (emission). Therefore, depending on the alignment of the molecules, $W_B > W_X$ can be achieved without net population inversion (i.e., $P_B < P_X$).

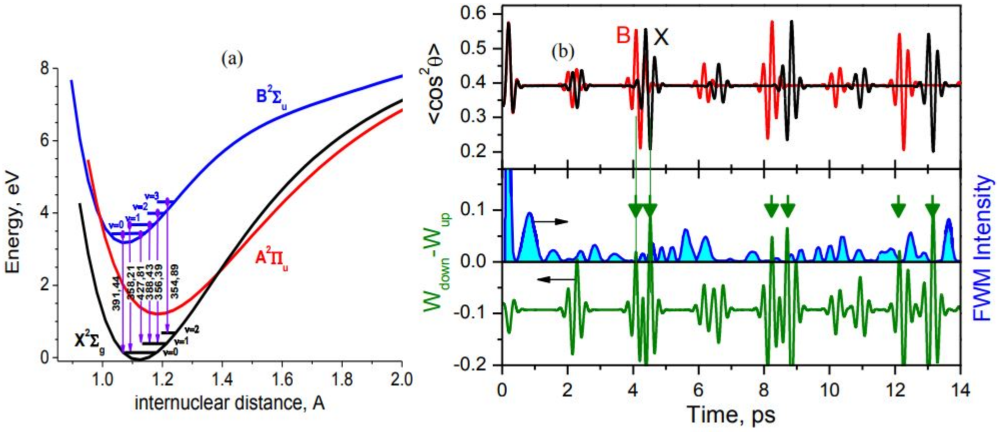

Figure 7.4: (a) Rovibronic UV transitions between the excited B and the ground X states in N_2^+. (b) Evolution of the rotational alignment factor $< cos^2(\theta(t)) >$, calculated probability difference between UV absorption and emission for $P_B = 3/4P_X$, and theoretical UV emission intensity due to four-wave mixing. Note that the positive peaks of the green curve correspond to ~100-fs-long transient gain windows that arise when the upper state B is well aligned while the ground state X is strongly delocalized. Courtesy of Ref. [11].

This gain mechanism predicts gain in short temporal windows during the rotational revivals of the molecules. However, it does not explain the fast decay of the gain as seen in our measurements and all previous pump-probe measurements from other groups. Therefore, if this mechanism plays a role, another mechanism needs to explain the gain between rotational alignment. Our experimental results (see Figure 6.3) suggest that this mechanism can play a role.

7.2.5 Rotational inversion

Another scheme to achieve optical gain without population inversion was proposed by A. Azarm et *al.*[92] and further investigated by M. Lei et *al.*[12].

They found that the pump pulse rotates the upper ($B^2\Sigma_u^+$) state differently than the lower ground ($X^2\Sigma_g^+$) state. Although, both works can't conclude that a net population inversion is not achieved, they confirm that a population inversion is possible between some rotational levels of the $B^2\Sigma_u^+$ and $X^2\Sigma_g^+$ state.

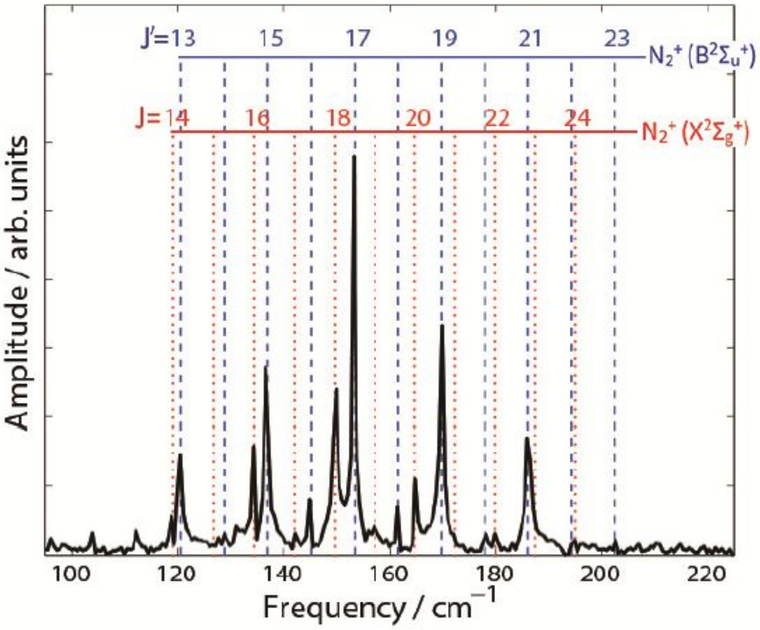

Figure 7.5: Fourier transformation of the time-dependent superradiance around 391 nm. Here J' and J are the rotation quantum number of the upper and lower states of the transition. The rotational coherence was clearly exhibited for both the excited state and the ground state of nitrogen molecular ions. Courtesy of Ref. [12].

Figure 7.5 shows the high frequency resolution Fourier transform analyzed by M. Lei et *al.* [12] from their time-domain evolution of the gain at 391 nm. They find that the population between rotational states J=13 and J=23 is 2.5 times larger in the $B^2\Sigma_u^+$ state than the $X^2\Sigma_g^+$ state.

7.3 Summary

I have revisited the main properties of N_2^+ lasing. Mainly the ultrafast build-up which suggests that strong field ionization is probably responsible for establishing gain in this system and the fast decay that seems to be due to electron collisions. Our experimental measurements suggests that the gain is superradiant and the evidence from other groups was discussed, solidifying this theory.

Some possible gain mechanisms that are based on population inversion were presented, such as electron recollision excitation, natural population inversion, and multiple state coupling. Our experiment suggest that recollision doesn't play a significant role in creating the inversion. Also, there is no experimental evidence of the concept of natural population inversion for this system. The inversion achieved by multiple state coupling seems to be the likely case if inversion is achieved. However, an inversion is created between the $A^2\Pi_u$ state and the $X^2\Sigma_g^+$ state, but no such lasing emission has been observed so far.

Other mechanisms not requiring a net population inversion was also presented. Inversion free transient gain predicts gain in a series of small windows during regions of molecular alignment. This mechanism does not explain the fast decay of the gain. However, gain due to inversion in a subset of rotational states seem to explain this decay since the distribution of rotational states can relax due to collisions.

Based on our experiment results, the gain mechanisms seem to be most likely "inversion free". Transient gain can explain the gain seen at the region of molecular revivals, persisting after the decay of the gain. While inversion between a subset of rotational states could explain this fast decay.

8 General conclusion and outlook

This thesis was dedicated to the study of the lasing emissions of the singly ionized nitrogen molecules pumped by femtosecond laser pulses. The two dominant emission lines emitting at 391 nm and 428 nm wavelengths that were studied belong to the transition between the $B^2\Sigma_u^+(\nu\text{'} = 0)$ and $X^2\Sigma_g^+(\nu = 0, 1)$ states. We started by studying the 428 nm emission in femtosecond filaments to link to previous work. We showed that the generated continuum that acts to self-seed the emissions doesn't explain the ellipticity behavior of the emissions. We then studied these emissions by focusing in a vacuum in a thin gas jet, thereby removing the complexity of filaments. This allowed us to make a direct comparison of the ellipticity dependence of the emissions and HHG, and we showed that recollision doesn't play a significant role in creating a population inversion between the states involved.

The following sections were dedicated to further understanding the mechanisms involved to achieve optical gain. We characterized the emissions by their temporal profile, gas jet position, and plasma density. The gain as a function of time shows an ultrafast gain buildup followed by a fast decay. We measured a strong rotational wavepacket that modulates the gain that depends on gas density. A cooler gas showed a clearer and stronger wavepacket. We also presented some evidence that electron collisions are likely the cause of the fast decay of the gain. We also found evidence of superradiance which is in agreement with previous work. This is an important measurement because it means that the seed pulse is not actually amplified and the emission occurs after the seed pulse left the system. The last set of measurements that we did showed that there's another mechanism present that depends on the alignment between the pump and probe. This will become of interest to the air lasing community because, in filaments, the two mechanisms would be indistinguishable. Finally, this thesis presented possible gain mechanisms taken from literature. Our results seem to indicate that a net population inversion is not achieved. More theoretical and experimental evidence will be required to make such conclusion.

One of the big problems with N_2^+ lasing is to achieve backward lasing for applications such as remote sensing. Backward lasing has been observed in N_2 and O_2, but the effect has yet to be reported for N_2^+. We propose the use of a zone plate to promote backward lasing. A zone plate has a wavelength dependent focusing distance. A properly chirped femtosecond pulse could create a backward traveling focus. I introduce the math in Appendix B as well as possible dimensions for such zone plates.

Air lasing has potential to revolutionize methods in remote sensing. Currently, the best methods analyze backscattered light from a remote target and require very sensitive equipment. However, many obstacles still stand in our way to make air lasing practical. First of all, after 7 years of research, we still don't understand the gain mechanism behind the N_2^+ air laser. Also, backward lasing would be the most practical emission direction but the forward emission seems to deplete the gain before backward lasing can occur. On top of these challenges, femtosecond laser sources are quite large, expensive, and not very mobile. This makes them very hard to use for remote sensing as we would need them at many locations. However, the costs and size of femtosecond lasers may eventually make this a feasible project. Furthermore, it's not obvious how to make the air laser useful at very large distances (several kilometers away). However, if the initial power of the laser beam is greater than the critical power for self-focusing the beam will self-focus, regardless of the initial beam size. Therefore, just by expanding a femtosecond laser beam we could generate filaments at larger distances but this would require very expensive optics. Finally, even with these obstacles, air lasing remains interesting not only for its potential application but also for the physics behind this lasing effect.

A Intensity calibration

A.1 MCP calibration

Before we can calibrate the intensity, we need to calibrate the MCP. To do so, we suppress the observed harmonics by changing the ellipticity of the driving laser to circular. This allows us to observe the fluorescence emitted from the nitrogen molecules. Figures A.1 (a) and (b) shows the fluorescence observed by the MCP.

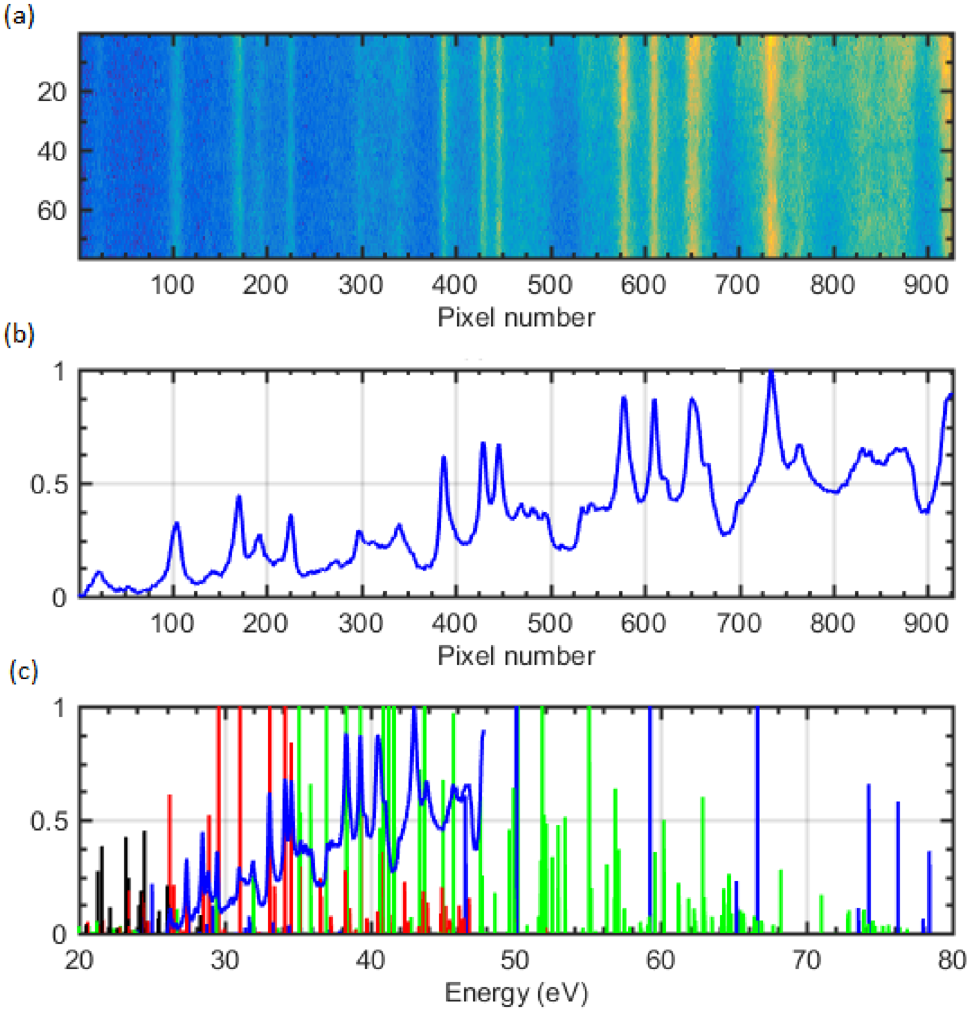

Figure A.1: (a) Emission lines from molecular nitrogen used for the MCP calibration as measured by the MCP. (b) Normalized intensity of the emission lines as a function of pixel number. (c) Emission lines from (b) calibrated with known emission lines of nitrogen.

The lines are then fitted using the known emission lines of N_2 (see Figure A.1 (c)). From this, we get a well-calibrated energy axis for the MCP.

A.2 Intensity calibration

The intensity is calibrated using the well-known cutoff law for HHG [75]:

$$E_{cutoff} = I_p + 3.17U_p \tag{A.1}$$

We take several spectra of the generated harmonics using different driving laser beam energies and identify the cutoff for each. The emitted harmonics are separated in energy by 3.1 eV because only the odd harmonics are generated. Knowing the harmonic order allows us to assign a cutoff energy E_{cutoff} and then U_p is then calculated using an ionization potential of 15.581 eV for N_2. U_p is given by Equation 5.2 and the intensity is related to the electric field by $I = c\epsilon_0 E_0^2/2$. The intensity is therefore given by:

$$I = \frac{2mc\epsilon_0\omega_0^2 U_p}{e^2}$$

B Fresnel Zone Plate

Unlike lenses, zone plates use diffraction to focus light. They consist of many rings, known as Fresnel zones as shown in Figure B.1. The rings alternate from opaque to transparent and are spaced in order to achieve constructive interference at a focus. Zone plates are often used to focus x-rays because glass only weakly refracts such light. In the following section, I derive the focal length of a zone plate to explain why it is of interest to us.

B.1 Focusing properties of the Fresnel Zone Plate

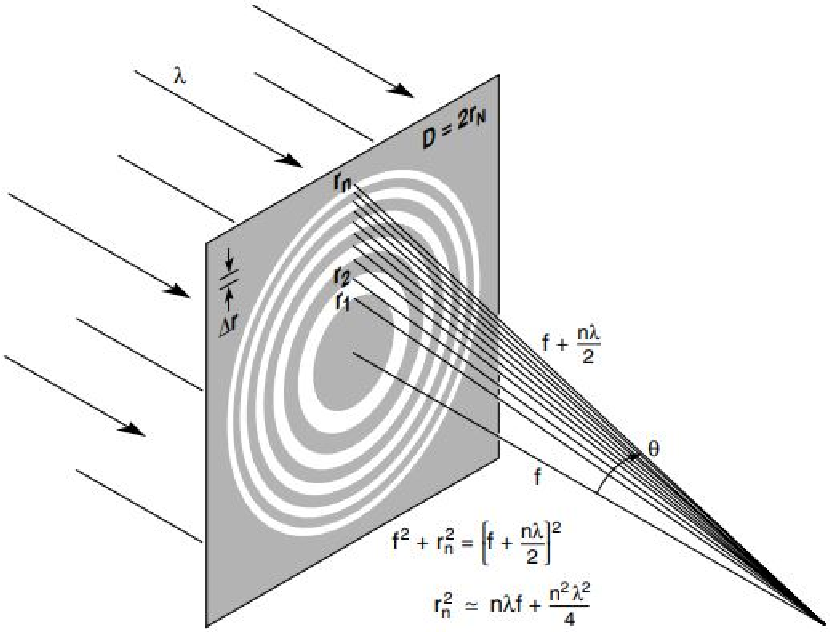

Figure B.1: A Fresnel zone plate showing the first order of diffraction. The nth zone radii is labeled r_n, the focusing distance is f, the outermost zone is Δr_N, and N is the total number of zones. Figure is taken from literature [13].

For constructive interference to occur we require that the distance from a zone to the focus f be $f + n\lambda/2$, where λ is the input wavelength. From Pythagorean Theorem we can write:

$$f^2 + r_n^2 = (f + \frac{n\lambda}{2})^2 \tag{B.1}$$

or,

$$r_n^2 = n\lambda f + \frac{n^2\lambda^2}{4} \tag{B.2}$$

Since we can set f such that $f >> \lambda$, we can neglect the $n^2\lambda^2/4$ term, and we get:

$$r_n^2 \approxeq n\lambda f \tag{B.3}$$

We can link this to the size of the outermost zone by taking the difference between the radii of the two outermost zones:

$$r_N^2 - r_{N-1}^2 = N\lambda f - (N-1)\lambda f = \lambda f \tag{B.4}$$

By defining the outermost zone width as:

$$\Delta r_N = r_N - r_{N-1} \tag{B.5}$$

Equation B.4 reduces to:

$$-\Delta r_N^2 + 2\Delta r_N r_N = \lambda f \tag{B.6}$$

Since $\Delta r_N \ll r_N$ we can get an equation for the focusing distance as a function of the zone plate radii r_N, the outermost zone width Δr_N, and the wavelength λ./

$$f = \frac{2r_N\Delta r_N}{\lambda} \tag{B.7}$$

B.2 Moving focus

Equation B.7 shows that the focusing distance of a zone plate is wavelength dependent. For a femtosecond chirped pulse, different wavelengths will focus at different distances as a function of time. Therefore we can rewrite the equation as:

$$z(\lambda(t)) = \frac{2r_N \Delta r_N}{\lambda(t)} \tag{B.8}$$

Where $z(\lambda(t))$ is the moving position of the focus as a function of time. Rewriting this equation in terms of frequency ν using $\lambda = \frac{c}{\nu}$ gives:

$$z(t) = \frac{2r_N \Delta r_N}{c} \nu(t) \tag{B.9}$$

Taking the derivative as a function of time on both sides we get a velocity for the moving focus:

$$\frac{dz(t)}{dt} = \frac{2r_N \Delta r_N}{c} \frac{d\nu(t)}{dt} \tag{B.10}$$

Now I can set the velocity to be $-c$ for a backward propagating focus traveling at the speed of light to obtain:

$$\frac{2r_N \Delta r_N}{c} \frac{d\nu(t)}{dt} = c \tag{B.11}$$

$$\frac{d\nu(t)}{dt} = \frac{-c^2}{2r_N \Delta r_N} \tag{B.12}$$

This is integrated to obtain:

$$\nu(t) = \nu_0 + \frac{-c^2}{2r_N \Delta r_N} t \tag{B.13}$$

or using the angular frequency $\omega = 2\pi\nu$:

$$\omega(t) = \omega_0 + \frac{-c^2\pi}{r_N \Delta r_N} t \tag{B.14}$$

This is similar to the instantaneous frequency described in Weiner's book [93]:

$$\omega_{inst}(t) = \omega_0 + \frac{d\phi(t)}{dt} = \omega_0 - 2\Gamma_i t = \omega_0 + \frac{2\beta t}{\alpha^2 + \beta^2} \tag{B.15}$$

Where Γ_i is the imaginary part of the pulse width parameter[93], and is related to the pulse duration and chirp. Setting these equations equal, I get

$$\frac{-c^2\pi}{r_N \Delta r_N} = \frac{2\beta}{\alpha^2 + \beta^2} \tag{B.16}$$

Where β is the chirp parameter and α is related to the pulse duration Δt by $\alpha = \Delta t^2/4log(2)$. Equation B16 is satisfied for $\Delta t = 100\ fs$, $\beta = -200\ fs^2$, $r_N = 1cm$, and $\Delta r_N = 19.5\mu m$.

References

[1] Jinping Yao, Bin Zeng, Huailiang Xu, Guihua Li, Wei Chu, Jielei Ni, Haisu Zhang, See Leang Chin, Ya Cheng, and Zhizhan Xu. High-brightness switchable multiwavelength remote laser in air. *Physical Review A*, 84:051802, Nov 2011.

[2] P. W. Dooley, I. V. Litvinyuk, Kevin F. Lee, D. M. Rayner, M. Spanner, D. M. Villeneuve, and P. B. Corkum. Direct imaging of rotational wave-packet dynamics of diatomic molecules. *Physical Review A*, 68(023406), 2003.

[3] A Couairon and A Mysyrowicz. Femtosecond filamentation in transparent media. *Physics Reports*, 441:47–189, 2007.

[4] Joshua E. Rothenberg. Space-time focusing: Breakdown of the slowly varying envelope approximation in the self-focusing of femtosecond pulses. *Optics Letters*, 17(19), 1992.

[5] Jerome Kasparian and Jean-Pierre Wolf. Physics and applications of atmospheric nonlinear optics and filamentation. *Optics Express*, 16(1), 2008.

[6] Yi Liu, Pengji Ding, Guillaume Lambert, Aurélien Houard, Vladimir Tikhonchuk, and André Mysyrowicz. Recollision-induced superradiance of ionized nitrogen molecules. *Physical Review Letters*, 115:133203, Sep 2015.

[7] P. B. Corkum and Ferenc Krausz. Attosecond science. *Nature Physics*, 3:381–387, 2007.

[8] M. Gross and S. Haroche. Superradiance: An essay on the theory of collective spontaneous emission. *Physics reports*, 93(5):301–396, 1982.

[9] Guihua Li, Chenrui Jing, Bin Zeng, Hongqiang Xie, Jinping Yao, Wei Chu, Jielei Ni, Haisu Zhang, Huailiang Xu, Ya Cheng, and Zhizhan Xu. Signature of superradiance from a nitrogen-gas plasma channel produced by strong-field ionization. *Physical Review A*, 89:033833, Mar 2014.

[10] Huailiang Xu, Erik Lotstedt, Atsushi Iwasaki, and Kaoru Yamanouchi. Sub-10-fs population inversion in n2+ in air lasing through multiple state coupling. *Nature Communications*, 6:8347, September 2015.

[11] D. Kartashov, S. Haessler, S. Aliasuskas, G. Andriukaitis, A. Pugzlys, A. Baltuska J. Mohring, D. Starukhin, M. Motzkus, A.M. Zheltikov, M. Richter, F. Morales, O. Smirnova, M. Yu. Ivanov, and M. Spanner. Transient inversion in rotationally aligned nitrogen ions in a femtosecond filament. *Research in Optical Sciences, page HTh4B.5*, 2014.

[12] Mingwei Lei, Chengyin Wu, An Zhang, Qihuang Gong, and Hongbing Jiang. Population inversion in the rotational levels of the superradiant n2 + pumped by femtosecond laser pulses. *Optics Express*, 25(4):4535–4541, Feb 2017.

[13] David Attwood. *Soft x-rays and extreme ultraviolet radiaion: principles and applications.* Cambridge university press, 1999.

[14] T.H. Mainman. Stimulated optical radiation in ruby. *Nature*, 187, 1960.

[15] Q. Luo, W. Liu, and S.L. Chin. Lasing action in air induced by ultra-fast laser filamentation. *Applied Physics B*, 76(3):337–340, 2003.

[16] Pengji Ding, Sergey Mitryukovskiy, Aurélien Houard, Eduardo Oliva, Arnaud Couairon, André Mysyrowicz, and Yi Liu. Backward lasing of air plasma pumped by circularly polarized femtosecond pulses for the sake of remote sensing (black). *Optics Express*, 22(24):29964–29977, Dec 2014.

[17] Pengji Ding, Eduardo Oliva, Aurelien Houard, Andre Mysyrowicz, and Yi Liu. Lasing dynamics of neutral nitrogen molecules in femtosecond filaments. *Physical Review A*, 94(043824), 2016.

[18] Peter W. Milonni and Joseph H. Eberly. *Laser Physics.* John Wiley & Sons, Inc., 2010.

[19] Bernard Valeur. *Molecular Fluorescence: Principles and Applications.* Wiley-VCH Verlag GmbH, 2001.

[20] B. H. Bransden and C. J. Joachain. *Quantum Mechanics: Second edition.* Pearson Education Ltd., 2000.

[21] Andrew Ellis, Miklos Feher, and Timothy Wright. *Electronic and photoelectron spectroscopy: fundamentals and case studies.* Cambridge University Press., 2005.

[22] M. Dantus, R. M. Bowman, and A. H. Zewail. Femtosecond laser observations of molecular vibration and rotation. *Letters to Nature*, 343:737–739, 1990.

[23] Ahmed H. Zewail. Femtochemistry: Atomic-scale dynamics of the chemical bond. *The Journal of Physical Chemistry A*, 104(24):5660–5694, 2000.

[24] R. L. Fork, B. I. Greene, and C. V. Shank. Generation of optical pulses shorter than 0.1 psec by colliding pulse mode locking. *Applied Physics Letters*, 38(671), 1981.

[25] P. F. Moulton. Spectroscopic and laser characteristics of $ti : al_2o_3$. *Journal of the Optical Society of America B*, 3, 1986.

[26] A.H. Zewail. *Femtochemistry: Ultrafast Dynamics of the Chemical Bond.* World Scientific, Singapoe, 1994.

[27] Jie Li, Xiaoming Ren, Yanchun Yin, Kun Zhao, Andrew Chew, Yan Cheng, Eric Cunningham, Yang Wang, Shuyuan Hu, Yi Wu, Michael Chini, and Zenghu Chang. 53-attosecond x-ray pulses reach the carbon k-edge. *Nature Communications*, 8(186), 2017.

[28] Philip R. Brooks, John S. McKillop, and H. Garry Poppin. Molecular beam reaction of k atoms with sideways oriented. *Chemical Physics Letters*, 66(1), 1979.

[29] Bretislav Friedrich and Dudley Herschbach. Alignment and trapping of molecules in intense laser fields. *Physical Review Letters*, 74(23), 1995.

[30] Bretislav Friedrich and Dudley Herschbach. Polarization of molecules induced by intense nonresonant laser fields. *The Journal of Physical Chemistry*, 99(42):15686–15693, 1995.

[31] Wousik Kim and Peter M. Felker. Spectroscopy of pendular states in optical-field-aligned species. *The Journal of Chemical Physics*, 104(1147), 1996.

[32] Tamar Seideman. Rotational excitation and molecular alignment in intense laser fields. *The Journal of Chemical Physics*, 103(7887), 1995.

[33] F Rosca-Pruna and M.J.J. Vrakking. Experimental observation of revival structures in picosecond laser-induced alignment of i_2. *Physical Review Letters*, 87(15), 2001.

[34] Robert W. Boyd. The intensity-dependent refractive index. In *Nonlinear Optics*. Academic Press, third edition, 2008.

[35] A.A. Askar'yan. Cerenkov radiation and transition radiation from electromagnetic waves. *Journal of Experimental and Theoretical Physics*, 15(5), 1962.

[36] R. Y. Chiao, E. Garmire, and C. H. Townes. Self-trapping of optical beams. *Physical Review Letters*, 13, 1964.

[37] P. L. Kelley. Self-focusing of optical beams. *Physical Review Letters*, 15(26):1005–1008, 1965.

[38] P. Lallemand and N. Bloembergen. Self-focusing of laser beams and stimulated raman gain in liquids. *Physical Review Letters*, 15:1010–1012, 1965.

[39] E. Garmire, R. Y. Chiao, and C. H. Townes. Dynamics and characteristics of the self-trapping of intense light beams. *Physical Review Letters*, 16:347–349, 1966.

[40] W. Liu and S.L. Chin. Direct measurement of the critical power of femtosecond ti:sapphire laser pulse in air. *Optics Express*, 13(15), 2005.

[41] E. L. Dawes and J. H. Marburger. Computer studies in self-focusing. *Physical Review Journals Archive*, 179, 1969.

[42] J. H. Marburger. Self-focusing: Theory. *Quantum Electronics*, 4:35–110, 1975.

[43] Gadi Fibich, Shmuel Eisenmann, Boaz Ilan, Yossi Erlich, Moshe Fraenkel, Zohar Henis, Alexander L. Gaeta, and Arie Zigler. Self-focusing distance of very high power laser pulses. *Optics Express*, 13(15):5897–5903, 2005.

[44] V. I. Talanov. Focusing of light in cubic media. *JETP Letters*, 11(6):199, 1970.

[45] F. DeMartini, C. H. Townes, T. K. Gustafson, and P. L. Kelley. Self-steepening of light pulses. *Physical Review Journals Archive*, 164, 1967.

[46] F. Bragheri, D. Faccio, A. Couairon, A. Matijosius, G. Tamosauskas, A. Varanavicius, V. Degiorgio, A. Piskarskas, , and P. Di Trapani. Conical-emission and shock-front dynamics in femtosecond laser-pulse filamentation. *Physical Review A*, 76, 2007.

[47] M. D. Feit and J. A. Fleck. Effect of refraction on spot-size dependence of laser-induced breakdown. *Applied Physics Letter*, 24, 1974.

[48] A. Braun, G. Korn, X. Liu, D. Du, J. Squier, and G. Mourou. Self-channeling of high-peak-power femtosecond laser pulses in air. *Optics Letters*, 20(1):73–75, Jan 1995.

[49] J. Kasparian, R. Sauerbrey, and S.L. Chin. The critical laser intensity of self-guided light filaments in air. *Applied Physics B*, 71:877–879, 2000.

[50] A. Becker, N. Akozbek, K. Vijayalakshmi, E. Oral, C.M. Bowden, and S.L. Chin. Intensity clamping and re-focusing of intense femtosecond laser pulses in nitrogen molecular gas. *Applied Physics B*, 73:287–290, 2001.

[51] Sergey Mitryukovskiy, Yi Liu, Pengji Ding, Aurélien Houard, Arnaud Couairon, and André Mysyrowicz. Plasma luminescence from femtosecond filaments in air: Evidence for impact excitation with circularly polarized light pulses. *Physical Review Letters*, 114:063003, Feb 2015.

[52] G. Mechain, C. D'Amico, Y.-B. Andre, S. Tzortzakis, M. Franco, B. Prade, A. Mysyrowicz, A. Couairon, E. Salmon, and R. Sauerbrey. Range of plasma filaments created in air by a multi-terawatt femtosecond laser. *Optics Communications*, 247:171–180, 2005.

[53] I. Golub. Optical characteristics of supercontinuum generation. *Optics Letters*, 15(6):305–307, 1990.

[54] E. T. J. Nibbering, P. F. Curley, G. Grillon, B. S. Prade, M. A. Franco, F. Salin, and A. Mysyrowicz. Conical emission from self-guided femtosecond pulses in air. *Optics Letters*, 21(1):62–64, 1996.

[55] P. Di Trapani, G. Valiulis, A. Piskarskas, O. Jedrkiewicz, J. Trull, C. Conti, and S. Trillo. Spontaneously generated x-shaped light bullets. *Physical Review Letters*, 91(093904), 2003.

[56] C. Conti, S. Trillo, P. Di Trapani, G. Valiulis, A. Piskarskas, O. Jedrkiewicz, and J. Trull. Nonlinear electromagnetic x-waves. *Physical Review Letters*, 90(170406), 2003.

[57] D. Faccio, MA Porras, A. Dubietis, F. Bragheri, A. Couairon, and P. Di Trapani. Conical emission, pulse splitting, and x-wave parametric amplification in nonlinear dynamics of ultrashort light pulses. *Physical Review Letters*, 19(193901), 2006.

[58] O. G. Kosareva, V. P. Kandidov, A. Brodeur, C. Y. Chien, and S. L. Chin. Conical emission from laser-plasma interactions in the filamentation of powerful ultrashort laser pulses in air. *Optics Letters*, 22(17):1332–1334, 1997.

[59] Qirong Xing, Kwong Mow Yoo, and Robert R. Alfano. Conical emission by four-photon parametric generation by using femtosecond laser pulses. *Applied Optics*, 32(12):2087–2089, 1993.

[60] G. G. Luther, A. C. Newell, and J. V. Moloney. Short-pulse conical emission and spectral broadening in normally dispersive media. *Optics Letters*, 19(11):789–791, 1994.

[61] S. L. Chin, H. L. Xu, Q. Luo, F. Theberge, W. Liu, J. F. Daigle, Y. Kamali, P. T. Simard, J. Bernhardt, S. A. Hosseini, M. Sharifi, G. Mejean, A. Azarm, C. Marceau, O. Kosareva, V. P. Kandidov, N. Akozbek, A. Becker, G. Roy, P. Mathieu, J. R. Simard, M. Chateauneuf, and

J. Dubois. Filamentation remote sensing of chemical and biological agents/pollutants using only one femtosecond laser source. *Applied Physics B*, 95(1):1–12, 2009.

[62] H. L. Xu and S. L. Chin. Femtosecond laser filamentation for atmospheric sensing. *Sensors*, 11(32), 2011.

[63] G. Andriukaitis, J. Mohring, D. Kartashov, and A. Baltuska. Intense, directional uv emission from molecular nitrogen ions in an adaptively controlled femtosecond filament. *EPJ Web of Conferences*, 41(10004), 2013.

[64] Jinping Yao, Guihua Li, Chenrui Jing, Bin Zheng, Wei Chu, Jielei Ni, Helong li, Ya Cheng, and Zhizhan Xu. Remote creation of coherent emissions in air with two-color ultrafast laser pulses. *New Journal of Physics*, 15, 2013.

[65] Jielei Ni, Wei Chu, Chenrui Jing, Haisu Zhang, and Zhizhan Xu. Identification of the physical mechanism of generation of coherent n_2^+ emissions in air by femtosecond laser excitation. *Optics Express*, 21(7):8746–8752, 2013.

[66] Yi Liu, Yohann Brelet, Guillaume Point, Aurélien Houard, and André Mysyrowicz. Self-seeded lasing in ionized air pumped by 800 nm femtosecond laser pulses. *Optics Express*, 21(19):22791–22798, Sep 2013.

[67] Wei Chu, Guihua Li, Hongqiang Xie, Jielei Ni, Jinping Yao, Bin Zeng, Haisu Zhang, Chenrui Jing, Huailiang Xu, Ya Cheng, and Zhizhan Xu. A self-induced white light seeding laser in a femtosecond laser filament. *Laser Physics Letters*, 11(1):015301, 2014.

[68] Tie-Jun Wang, Jean-Francois Daigle, Jingjing Ju, Shuai Yuan, Ruxin Li, and See Leang Chin. Forward lasing action at multiple wavelengths

seeded by white light from a femtosecond laser filament in air. *Physical Review A*, 88, 2013.

[69] Guillaume Point, Yi Liu, Yohann Brelet, Sergey Mitryukovskiy, Pengji Dingand Aurelien Houard, and Andre Mysyrowicz. Lasing of ambient air with microjoule pulse energy pumped by a multi-terawatt infrared femtosecond laser. *Optics Letters*, 39(7), 2014.

[70] H. Zhang, C. Jing, G. Li, H. Xie, J. Yao, B. Zeng, W. Chu, J. Ni, H. Xu, and Y. Cheng. Abnormal dependence of strong-field-ionization-induced nitrogen lasing on polarization ellipticity of the driving field. *Physical Review A*, 88(6):063417, December 2013.

[71] Khan Lim, Magali Durand, Matthieu Baudelet, and Martin Richardson. Transition between linear and nonlinear focusing regimes during filamentation. In *CLEO: 2015*, page FTu4D.4. Optical Society of America, 2015.

[72] Shermineh Rostami, Michael Chini, Khan Lim, John P. Palastro, Magali Durand, Jean-Claude Diels, Ladan Arissian, Matthieu Baudelet, and Martin Richardson. Dramatic enhancement of supercontinuum generation in elliptically-polarized laser filaments. *Scientific Reports*, 6:20363, February 2016.

[73] V. Loriot, E. Hertz, O. Faucher, and B. Lavorel. Measurement of high order kerr refractive index of major air components. *Optics Express*, 17(16):13429, 2009.

[74] P. B. Corkum. Plasma perspective on strong field multiphoton ionization. *Physical Review Letters*, 71:1994–1997, Sep 1993.

[75] Jeffrey L. Krause, Kenneth J. Schafer, and Kenneth C. Kulander. High-order harmonic generation from atoms and ions in the high intensity regime. *Physical Review Letters*, 68(24), 1992.

[76] K. S. Budil, P. Salieres, A. L'Huillier, T. Ditmire, and M. D. Perry. Influence of ellipticity on harmonic generation. *Physical Review A*, 48(2), 1993.

[77] P. Dietrich, N. H. Burnett, M. Ivanov, and P. B. Corkum. High-harmonic generation and correlated two-electron multiphoton ionization with elliptically polarized light. *Physical Review A*, 50, 1994.

[78] Mathew Britton, Patrick Laferriere, Dong Hyuk Ko, Zhengyan Li, Fanqi Kong, Graham Brown, Andrei Naumov, Chunmei Zhang, Ladan Arissian, and P. B. Corkum. Testing the role of recollision in n_2^+ air lasing. *Physical Review Letters*, 120(133208), 2018.

[79] Haisu Zhang, Chenrui Jing, Jinping Yao, Guihua Li, Bin Zeng, Wei Chu, Jielei Ni, Hongqiang Xie, Huailiang Xu, See Leang Chin, Kaoru Yamanouchi, Ya Cheng, and Zhizhan Xu. Rotational coherence encoded in an "air-laser" spectrum of nitrogen molecular ions in an intense laser field. *Physical Review X*, 3:041009, Oct 2013.

[80] Xunqi Zhong, Zhiming Miao, Linlin Zhang, Qingqing Liang, Mingwei Lei, Hongbing Jiang, Yunquan Liu, Qihuang Gong, and Chengyin Wu. Vibrational and electronic excitation of ionized nitrogen molecules in intense laser fields. *Physical Review A*, 96(043422), 2017.

[81] Xunqi Zhong, Zhiming Miao, Linlin Zhang, Hongbing Jiang, Yunquan Liu, Qihuang Gong, and Chengyin Wu. Optimizing the 391-nm lasing intensity from ionized nitrogen molecules in 800-nm femtosecond laser fields. *Physical Review A*, 97(033409), 2018.

[82] L Klynning and P Pages. The band spectrum of n_2^+. *Physica Scripta*, 25(4):543–560, 1982.

[83] Ladan Arissian, Brian Kramer, Ali Rastegari, David Villeneuve, and Jean Claude Diels. Transient gain from n_2^+ in light filaments. 2018.

[84] G. Yu. Golubiatnikov and A. F. Krupnov. Molecular constants of the ground state of oxygen ($^{16}o^2$) accounting for new experimental data. *Journal of Molecular Spectroscopy*, 2004.

[85] Jorgen Bendtsen and Finn Rasmussen. High-resolution incoherent fourier transform raman spectrum of the fundamental band of $^{14}n^2$. *Journal of Raman Spectroscopy*, 2000.

[86] Jielei Ni, Wei Chu, Haisu Zhang, Chenrui Jing, Jinping Yao, Huailiang Xu, Bin Zeng, Guihua Li, Chaojin Zhang, See Leang Chin, Ya Cheng, and Zhizhan Xu. Harmonic-seeded remote laser emissions in n2-ar, n2-xe and n2-ne mixtures: a comparitive study. *Optics Express*, 20(19):20970–20979, 2012.

[87] Daniil Kartashov, Skirmantas Ališauskas, Audrius Pugžlys, Mikhail N Shneider, and Andrius Baltuška. Theory of a filament initiated nitrogen laser. *Journal of Physics B: Atomic, Molecular and Optical Physics*, 48(9):094016, 2015.

[88] Mingwei Lei, Chengyin Wu, and Hongbing Jiang. The fast decay of ionized nitrogen molecules in laser filamentation investigated by a picosecond streak camera. *Jornal of Physics B, Atomic, Molecular and Optical Physics*, 50, 2017.

[89] R.H. Dicke. Coherence in spontaneous radiation processes. *Physical Review*, 93(1), 1954.

[90] See Leang Chin, Huailiang Xu, Ya Cheng, Zhizhan Xu, and Kaoru Yamanouchi. Natural population inversion in a gaseous molecular filament. *Chinese Optics Letters*, 11(1):013201, 2013.

[91] Jinping Yao, Shicheng Jiang, Wei Chu, Bin Zeng, Chengyin Wu, Ruifeng Lu, Ziting Li, Hongqiang Xie, Guihua Li, Chao Yu, Zhanshan Wang,

Hongbing Jiang, Qihuang Gong, and Ya Cheng. Population redistribution among multiple electronic states of molecular nitrogen ions in strong laser fields. *Physical Review Letters*, 116, 2016.

[92] Ali Azarm, Paul Corkum, and Pavel Polynkin. Optical gain in rotationally excited nitrogen molecular ions. *Physical review A*, 96, 2017.

[93] Andrew M. Weiner. *Ultrafast Optics*. John Wiley & Sons, Inc., Hoboken, New Jersey., 2009.